

Ge and Si isotope signatures in rivers: A quantitative multi-proxy approach

Baronas Jokubas Jotautas^{1,*}, Torres Mark A.¹, West A. Joshua¹, Rouxel Olivier², Georg Bastian³,
Bouchez Julien⁴, Gaillardet Jérôme⁴, Hammond Douglas E.¹

¹ Department of Earth Sciences, University of Southern California, Los Angeles, CA 90089, USA

² Institut Français de Recherche pour l'Exploitation de la Mer, Centre de Brest, Technopôle Brest Iroise, 29280 Plouzané, France

³ Water Quality Centre, Trent University, Peterborough, ON K9L 1Z8, Canada

⁴ Institut de Physique du Globe de Paris (IPGP), Sorbonne Paris Cité, University Paris Diderot, CNRS, Paris 75231, France

* Corresponding author : Jokubas Jotautas Baronas, email address : jotautas.baronas@gmail.com

Abstract :

Solutes derived from the dissolution of silicate minerals play a key role in Earth's climate via the carbon and other biogeochemical cycles. Silicon (Si) is a unique constituent of silicate minerals and a biologically important nutrient, so tracing its behavior in near-surface environments may provide important insights into weathering processes. However, Si released by weathering is variably incorporated into secondary mineral phases and biota, obscuring signals derived from primary weathering processes. Due to chemical similarities, Germanium (Ge) may help better understand the Si cycle and its relationship to chemical weathering. With this aim, we report new measurements of the concentration and isotopic composition of Ge for both the dissolved and particulate phases of a variety of global rivers. These measurements are combined with analyses of concentration and isotopic ratio of Si on the exact same sample set in order to make direct comparisons of the behavior of these two elements in natural river systems. With this dataset, we develop a new modeling framework describing the full elemental and isotopic systems of these solutes in rivers (i.e., Ge/Si, $\delta^{74}\text{Ge}$, and $\delta^{30}\text{Si}$). This multi-proxy approach allows us to ascertain the relative importance of biological versus mineral uptake in modulating the fluxes of these elements delivered to the modern ocean. Dissolved $\delta^{74}\text{Ge}$ composition of rivers studied thus far range from 0.9 to 5.5 ‰ with a discharge-weighted global average of 2.6 ± 0.5 ‰. The Ge isotope composition of riverine suspended and bedload sediments is indistinguishable from silicate source rocks, which is consistent with mass balance expectations. The multi-proxy modeling suggests that, among the watersheds studied here, the isotopic fractionation of Si during secondary mineral phase precipitation ($\Delta^{30}\text{Sisec}$) ranges from -2.7 to -0.2 ‰, which removes between 19-79% of the initial dissolved Si sequestration, while between 12-54% is incorporated by biota. For Ge, modeling indicates that 79-98% of the dissolved load is incorporated into secondary mineral phases with a $\Delta^{74}\text{Gesec}$ ranging from -4.9 to -0.3 ‰. The fractionation induced by biological uptake is calculated to range from -2.6 to -1.3 ‰ for $\Delta^{30}\text{Sibio}$ and -0.7 ± 0.7 ‰ for $\Delta^{74}\text{Gebio}$. In addition to improving our understanding of the coupled Ge and Si cycles, our study provides a framework for

using multiple isotopic tracers to elucidate the chemical behavior of solutes in natural waters

Highlights

► Ge and Si isotope composition of water and sediments in various rivers is presented. ► Dissolved $\delta^{74}\text{Ge}$ range 0.9–5.5‰, river sediment $\delta^{74}\text{Ge}$ range 0.5–0.7‰. ► Dissolved $\delta^{74}\text{Ge}$ is strongly fractionated due to low chemical Ge mobility. ► Ge/Si-isotope multi-proxy provides quantitative constraints on secondary vs biological fractionation.

Keywords : germanium, silicon, isotope, rivers, weathering, fractionation

1 Introduction

Chemical weathering of rocks determines nutrient supply to ecosystems, landscape evolution, and climate over geological timescales. Understanding weathering processes is challenging in the contemporary environment and even more so in the past. Elemental and isotopic ratios of weathering-derived chemical species in waters and sediments can indirectly trace the myriad of water-rock-life interactions that take place in the critical zone, helping unravel solute sources and biogeochemical transformations. Moreover, the signatures of these proxies preserved in the sedimentary record offer the potential to reconstruct key aspects of weathering systems in the past and to test a variety of hypotheses linking weathering and climate (e.g., Berner et al., 1983; Raymo & Ruddiman, 1992).

With this in mind, a number of elemental and isotopic proxies, such as germanium to silicon ratios (Ge/Si), as well as multiple metal and metalloid stable isotope ratios, have been investigated (e.g., Murnane & Stallard, 1990; Dellinger et al., 2015; Tipper et al., 2012; Frings et al., 2016).

Although these isotopic proxies have alluring potential to improve our understanding of the effects of climatic forcing on critical zone processes, most field studies to date have focused on "calibrating" the proxies, i.e. understanding their isotopic behavior, within the context of biogeochemical processes established via alternative (often conventional) geochemical and geophysical techniques (e.g., von Blanckenburg & Schuessler, 2014; Meek et al., 2016).

Due to the defined boundaries of river catchments, mass balance constraints can be applied in studies of weathering tracers in river water. A mass balance approach can potentially provide quantitative information on the biogeochemical processes that fractionate the tracer of interest (Georg et al., 2006a; Bouchez et al., 2013). However, the associated uncertainties are large due to poor constraints on elemental and isotopic fractionation factors, which can be highly dependent on mineralogy, climate, ecosystem dynamics, or other aspects of the studied watershed (e.g., Wimpenny et al., 2015; Frings et al., 2016). As a result, most isotope weathering studies to date have focused on empirically calibrating isotopic fractionation factors, rather than using the isotopic information to assess the underlying biogeochemical processes (e.g., Hughes et al., 2013; Dellinger et al., 2015; Baronas et al., 2017a).

Here, we explore the range of Ge and Si isotopic and elemental signatures in a number of global rivers. Germanium isotopes ($\delta^{74}\text{Ge}$) have recently been shown to fractionate in terrestrial systems (Baronas et al., 2017a). In this study, we present new coupled data on $\delta^{74}\text{Ge}$, $\delta^{30}\text{Si}$, and Ge/Si. Dissolved and particulate data from the headwaters of the Amazon river system reveal that the Ge and Si systems have distinct isotopic behavior, despite their chemical affinity. Coupling these systems thus provides the opportunity to distinguish between biological and secondary phase controls on the Si cycle. We describe a simple multi-proxy model to quantitatively distinguish between the uptake and fractionation of these two elements between organic (biological) and inorganic (secondary mineral / amorphous) phases. This study significantly expands on the previous riverine $\delta^{74}\text{Ge}$ dataset (Baronas et al., 2017a), and now includes more of the world's major rivers ($n = 6$, allowing for revised estimates of the global riverine composition), as well as the first suspended and bed load sediment $\delta^{74}\text{Ge}$ data.

2 Methods

2.1 Sample collection

The sample set presented in this study covers a wide range of terrestrial environments, from tropical lowlands, to steep mountain catchments, to glacier-fed streams (Fig. 1). In particular, a number of dissolved and solid samples were collected along the Andes-Amazon elevation gradient in Peru, where previous studies on the geomorphic effects on weathering (Torres et al., 2015, 2016, 2017; Baronas et al., 2017b) provide a detailed context for the interpretation of Ge and Si isotope data.

Due to low dissolved Ge concentrations, 0.5-3 L of river water is needed to obtain >2 ng of Ge required for a $\delta^{74}\text{Ge}$ measurement. The data set presented here consists of samples collected over several years (Table 1). All samples were collected in plastic bottles or bags, filtered (0.2-0.45 μm), generally within ~24 h or less, and usually acidified with trace clean HCl or HNO₃ shortly thereafter. Tests showed that acidification is not required to keep Ge and Si in solution (except possibly in very Fe-rich samples) and no effect of filter pore size on Ge or Si composition. The

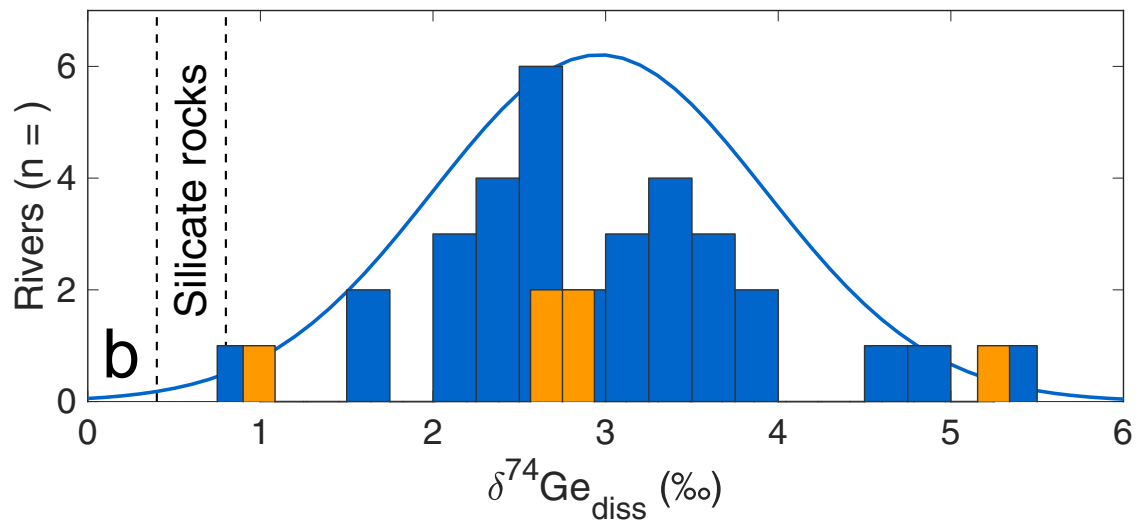
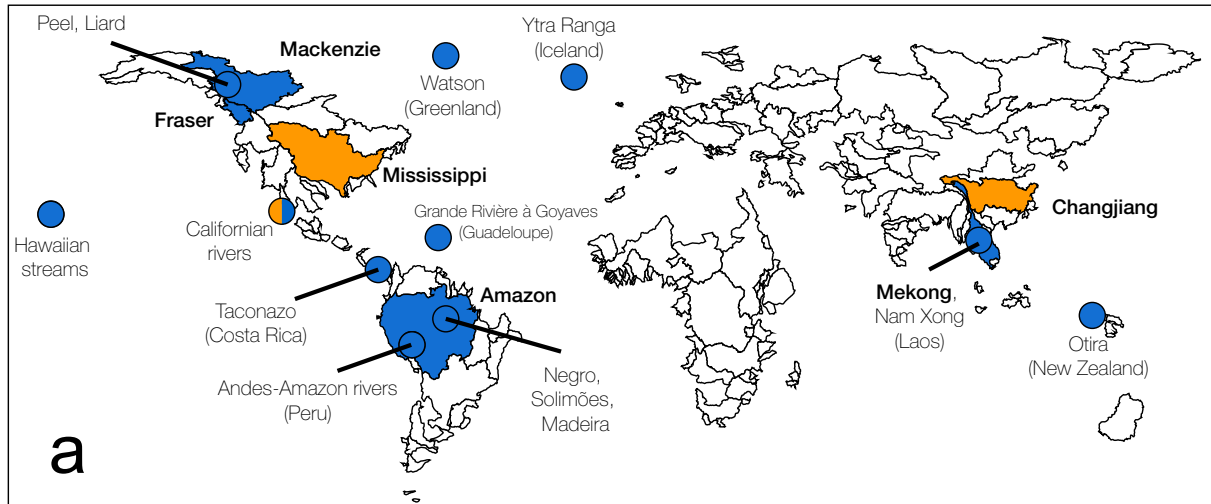


Figure 1: A map of major river basins (exorheic areas only), showing the locations of rivers and streams for which Ge isotope data are now available (panel a). World's major river basins are outlined. Smaller rivers and streams are shown as circles. Also shown a histogram of dissolved riverine $\delta^{74}\text{Ge}$ values (b). Blue color indicates primarily pristine rivers, whereas orange color indicates catchments with major anthropogenic perturbation (see Table 1). The solid blue line in panel b shows a normal distribution fit to the pristine riverine data. The range of silicate rock values (Rouxel & Luais, 2017) is denoted by vertical dashed lines. The map is based on WRIBASIN data and was obtained from <http://www.fao.org/geonetwork/srv/en/metadata.show?id=30914>.

collection of bedload samples in Peru is described in Torres et al. (2016). For suspended load samples, the sediment was either rinsed off filters with deionized water, centrifuged, and dried, or gently scraped off after drying the filter at 50-60 °C.

2.2 Chemical analyses

A detailed description of all sample preparation and analytical methods is given in Appendix A. Briefly, Si concentrations in solid samples were determined either via ICP-MS after acid digestion or via colorimetry after NaOH fusion. Ge concentrations in solid samples were determined after acid digestion on isotopically spiked aliquots purified for $\delta^{74}\text{Ge}$ analyses (see below), via hydride generation (HG)-ICP-MS. Two different digestion methods have been tested for both Si and Ge analyses, and the obtained values are compared in Table 2. In addition, a number of certified and previously measured reference materials were analyzed for Si, Ge, $\delta^{30}\text{Si}$, and $\delta^{74}\text{Ge}$ using the different digestion methods. The results of this study agreed well with previously reported values and were reproducible using either of the different digestion methods (Appendix Table A3).

Dissolved major cation and Si concentrations were measured using MP-OES (Agilent 4100). Additional Si analyses were done using molybdate blue colorimetry. Dissolved Ge concentrations were measured using isotope dilution HG-ICP-MS (Baronas et al., 2016).

Si isotope analyses were performed using MC-ICP-MS after cation-exchange chromatographic separation, adapting the method of Georg et al. (2006b). Measurements were done on a Thermo Neptune in medium resolution mode (resolving power $m/\Delta m = 4000$) using the Elemental Scientific Instruments Apex interface, at the flat part of the interference-free peak shoulder. Sample runs were bracketed with concentration-matched NBS-28 standard solution and the $\delta^{30}\text{Si}$ values are reported in ‰ as $^{30}\text{Si}/^{28}\text{Si}$ sample ratio normalized to the average $^{30}\text{Si}/^{28}\text{Si}$ ratio of bracketing NBS-28 measurements. Signal sensitivity ranged between 6-13 V/ppm ^{28}Si (60-130 pA on a $10^{11}\Omega$ amplifier), with each measurement integrated over 4 min and 4-8 replicate bracketed measurements. The possible interference from dissolved organic compounds was tested by digesting several samples (including Rio Negro) with conc. H_2O_2 prior to chromatography, which yielded $\delta^{30}\text{Si}$ values identical to untreated samples, suggesting that any potential matrix effects are negligible.

Ge isotope analyses were performed using HG-MC-ICP-MS after double isotope spiking (spike $^{73}\text{Ge}/^{70}\text{Ge} = 1$, spike/sample Ge mass ratio = 1-2) and anion-exchange chromatographic separation, adapting the method of Rouxel et al. (2006) and Guillermic et al. (2017). After double spiking but prior to column separation, dissolved Ge in river water samples was pre-concentrated by co-precipitating with Fe oxyhydroxides, settling and centrifuging, and re-dissolving the precipitate in HNO_3 . Measurements were done on a Thermo Neptune in low resolution mode, using a CETAC HGX-200 hydride generation interface. Each analysis was performed for 8-10 min at a signal intensity of 0.4-6V (4-60 pA on a $10^{11}\Omega$ amplifier) at ^{74}Ge . Sample runs were bracketed with concentration- and spike/sample ratio-matched NIST-3120a standard solution. The $\delta^{74}\text{Ge}$ values were calculated using the double-spike data reduction routine of Siebert et al. (2001) and are reported in ‰ as $^{74}\text{Ge}/^{70}\text{Ge}$ sample ratio normalized to the average $^{74}\text{Ge}/^{70}\text{Ge}$ ratio of bracketing NIST 3120a measurements. There are major differences between the method used in the current study and the one previously employed by Baronas et al. (2017a) to make the first river $\delta^{74}\text{Ge}$ measurements (a detailed comparison is given in Appendix Table A2). To ensure reproducibility, a number of river samples previously analyzed by Baronas et al. (2017a) were re-analyzed in this study, giving identical results within uncertainty (Table 1).

The $\delta^{30}\text{Si}$ and $\delta^{74}\text{Ge}$ measurement uncertainty is reported as the external 2σ standard error of replicate measurements, or the 2σ standard deviation of all bracketing standard measurements within a given analytical session, whichever is higher.

3 Results and discussion

3.1 Ge and Si isotope composition of river-transported solids in the Andes-Amazon system

First and foremost, the Ge isotope composition of rock, bedload, and suspended load samples falls in the narrow 0.5-0.7 ‰ range (Table 2, Fig. 2) and is indistinguishable from various rocks analyzed previously (Rouxel et al., 2006; Escoubé et al., 2012; Rouxel & Luais, 2017). Such $\delta^{74}\text{Ge}$ homogeneity in solids is in stark contrast with other isotopic weathering tracers, such as $\delta^{30}\text{Si}$ and $\delta^7\text{Li}$ (Frings et al., 2016; Dellinger et al., 2014, 2017).

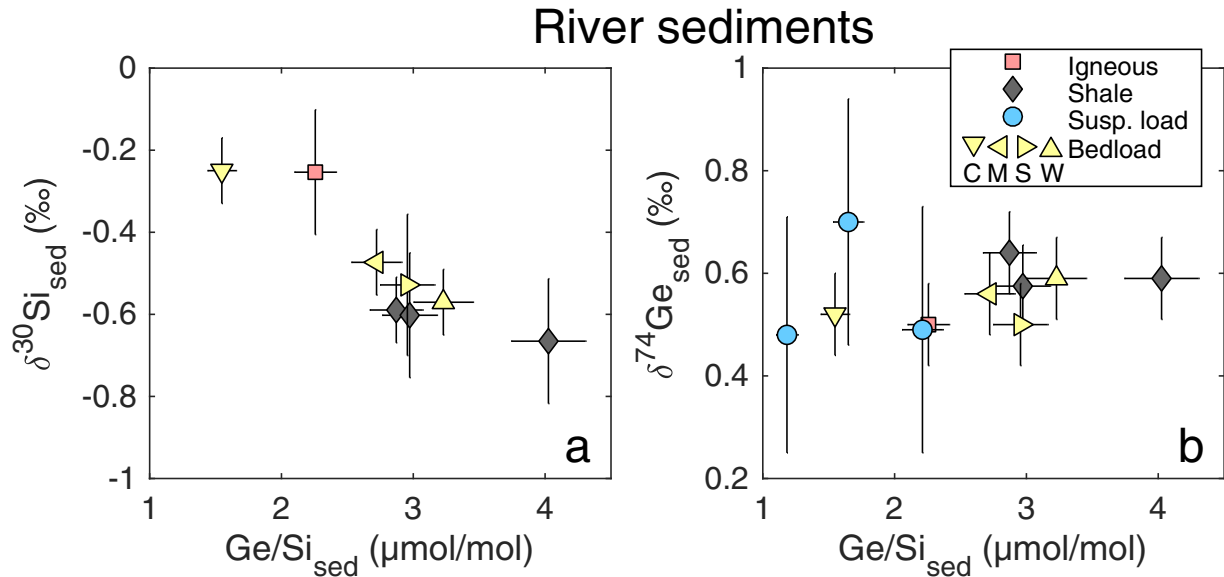


Figure 2: The relationship between rock and river sediment Ge/Si vs. $\delta^{30}\text{Si}$ (a) and $\delta^{74}\text{Ge}$ (b) in the Andes-Amazon. Site naming convention retained from Torres et al. (2015) and Torres et al. (2016) (the latter in parentheses): W = Kosñipata riv. at Wayqecha (Mountain-1); S = Kosñipata at Sen Pedro (Mountain-2); M = Alto Madre de Dios riv. at MLC (Mountain-front); C = Madre de Dios river at CICRA (Foreland-floodplain).

A set of river sediment samples spanning the geomorphic gradient from the Andes mountains to the Amazon floodplain was analyzed to investigate the effect of different erosional regimes on river sediment $\delta^{74}\text{Ge}$, $\delta^{30}\text{Si}$, and Ge/Si composition. The Andean shales and bedloads are enriched in light Si isotopes (-0.67 to -0.18 ‰) relative to igneous rocks (which typically range from -0.3 to 0.3 ‰ (Savage et al., 2013)) and exhibit elevated Ge/Si ratios (Fig. 2a), likely due to previous episodes of weathering or marine authigenesis preceding metamorphism and exhumation. This behavior is analogous to that observed for $\delta^7\text{Li}$, with shales found to be isotopically lighter due to inheritance from prior weathering (Dellinger et al., 2014, 2017). It may therefore seem surprising that these rocks retain the original primary $\delta^{74}\text{Ge}$ composition of about 0.6 ‰ (Fig. 2b), given that Ge isotope fractionation occurs both during weathering (Baronas et al. (2017a); see also Section 3.2) and during marine sediment authigenesis (Baronas, 2017). These results are however consistent with the study of Rouxel et al. (2006) showing that deep sea marine clays have $\delta^{74}\text{Ge}$ values

identical to bulk silicate Earth. The negligible Ge isotopic fractionation of the solids is a result of the low chemical mobility of Ge, i.e., strong retention during clay neof ormation, as indicated by continuously increasing clay Ge/Si ratios with continued weathering (Kurtz et al., 2002). The undetectable $\delta^{74}\text{Ge}$ fractionation of river-transported sediments is therefore qualitatively consistent with the conceptual model of Bouchez et al. (2013), given that typically only a small portion of Ge (<1-2 %) is exported in dissolved form. The behavior of $\delta^{74}\text{Ge}$ in this case contrasts with that of $\delta^{30}\text{Si}$ and $\delta^7\text{Li}$ systems, where the neof ormed clays are often strongly depleted in heavier isotopes relative to primary silicates, because a significant proportion of these elements (often upwards of 10 %) is exported in dissolved form (Gaillardet et al., 2014, also see Section 3.3.2).

Table 1: Sample details, dissolved Ge and Si concentrations, and isotopic compositions in the world's rivers studied here.

River	Sample ID	Sampling location	Time sampled	Lat., °	Long., °	Dom. lith. **	Ge, pmol/L	Si, $\mu\text{mol/L}$	Ge/Si, $\mu\text{mol/mol}$	$\delta^{74}\text{Ge}$, ‰	$\delta^{30}\text{Si}$, ‰	
										<i>this study</i>	<i>Baronas et al. (2017a)</i>	
<u>North America</u>												
Mississippi* (Aug 2011)	MI11	New Orleans, USA	2011-08-20	29.954	-90.063	mixed	266	166	1.60	2.17 ± 0.24	2.01 ± 0.22	--
Mississippi* (Jul 2015)	GRO001622	New Orleans, USA	2015-07-07	29.920	-90.140	mixed	215	147	1.46	2.60 ± 0.30	--	1.70 ± 0.15
Kaweah	KW13	Sierra Nevada mts., USA	2013-08-31	34.680	-118.840	gran.	690	210	3.29	2.32 ± 0.07	--	--
Lone Pine Creek	LPC13	Sierra Nevada mts., USA	2013-08-17	36.595	-118.140	gran.	94	164	0.57	2.46 ± 0.24	--	--
Kern (North Fork)	KN09	Sierra Nevada mts., USA	2009-03-21	35.916	-118.444	mixed	614	327	1.88	2.70 ± 0.25	2.75 ± 0.22	--
Kern* (Lower)	KL09	Sierra Nevada mts., USA	2009-03-21	35.916	-118.444	gran.	299	36	8.31	2.56 ± 0.24	3.04 ± 0.22	4.23 ± 0.20
San Gabriel (North Fork)	SGN13	San Gabriel mts., USA	2013-07-28	34.343	-117.725	gran.	68	256	0.27	5.20 ± 0.24	5.61 ± 0.22	2.13 ± 0.15
Santa Clara	SC13	San Gabriel mts., USA	2013-12-19	34.348	-119.052	sed.	205	414	0.50	3.38 ± 0.08	--	--
Hondo*	RH08	Los Angeles, USA	2008-12-20	34.098	-118.021	urban	172	290	0.59	5.17 ± 0.24	5.50 ± 0.22	--
Los Angeles River*	LAR13	Los Angeles, USA	2013-11-21	33.804	-118.205	urban	4011	155	25.9	0.93 ± 0.43	--	--
Mackenzie	CAN10-(11+14)	Tsiigehtchic, Canada	2010-09-07	67.458	-133.727	mixed	64	65	0.98	2.57 ± 0.09	--	1.15 ± 0.15
Liard	CAN10-(46+48)	Fort Simpson, Canada	2010-09-13	61.823	-121.298	mixed	55	89	0.62	2.76 ± 0.22	--	0.96 ± 0.22
Peel	CAN10-(03+05)	Fort McPherson, Canada	2010-09-07	67.430	-134.906	sed.	76	62	1.22	3.30 ± 0.09	--	0.96 ± 0.15
Fraser	FR15	Fort Langlely, Canada	2013-09-30	49.180	-122.567	gran.	39	77	0.51	1.67 ± 0.28	--	1.12 ± 0.15
<u>Greenland</u>												
Watson	JO-14	Kangerlussuaq, Greenland	2014-08-27	67.010	-50.682	gneiss	55	33	1.66	0.86 ± 0.24	--	-0.12 ± 0.15
<u>Volcanic islands</u>												
Waimano	OA14-1	Oahu, Hawai'i	2014-03-01	21.433	-157.922	bas.	47	201	0.24	2.05 ± 0.28	--	--
Uhva	OA14-2	Oahu, Hawai'i	2014-03-01	21.485	-157.871	bas.	91	492	0.19	3.53 ± 0.28	--	0.86 ± 0.15
Kahaua	OA14-3	Oahu, Hawai'i	2014-03-01	21.548	-157.877	bas.	198	399	0.50	2.54 ± 0.28	--	--
Molokai	ML09	Molokai, Hawai'i	2009-03-29	21.141	-157.015	bas.	809	823	0.98	2.61 ± 0.24	2.33 ± 0.22	--
Iao Valley	MA09	Maui, Hawai'i	2009-03-31	20.876	-156.557	bas.	120	354	0.34	3.17 ± 0.24	3.63 ± 0.22	--
Ytra Ranga	YR15	Hella, Iceland	2015-08-05	63.846	-20.394	bas.	273	364	0.75	3.97 ± 0.23	--	1.13 ± 0.15
Grande Riviere de Goyave	AN-14-(42-44)	Basse-Terre, Guadeloupe	2014-06-14	16.205	-61.654	bas.	77	366	0.21	3.59 ± 0.23	--	1.22 ± 0.15
<u>Asia & Oceania</u>												
Changjiang* (Nov 2014)	CJ14	Nanjing, China	2014-11-12	32.016	118.676	mixed	262	131	2.00	2.72 ± 0.24	--	--
Changjiang* (Jan 2015)	CJ15	Nanjing, China	2015-01-10	32.016	118.676	mixed	264	121	2.18	2.50 ± 0.24	--	--
Mekong	ME14	Luang Prabang, Laos	2014-03-29	19.896	102.136	sed.	240	171	1.41	2.91 ± 0.24	--	--
Nam Xong	NX14	Vang Vieng, Laos	2014-04-01	18.922	102.445	sed.	84	305	0.28	3.90 ± 0.11	--	--
Otira	OT14	Southern Alps, New Zealand	2015-01-31	-42.851	171.560	sed.	233	66	3.54	1.61 ± 0.24	--	--
<u>Central & South America</u>												
Taconazo	LS01	La Selva, Costa Rica	2010-05-14	10.432	-84.013	bas.	107	120	0.89	2.58 ± 0.12	--	0.29 ± 0.13
Kosñipata (Aug 2013)	MMD-02	Andes mts., Peru	2013-08-11	-13.058	-71.545	sed.	90	236	0.38	--	4.96 ± 0.22	0.94 ± 0.15
Kosñipata (Oct 2015)	KOS15	Andes mts., Peru	2015-10-25	-13.058	-71.545	sed.	76	192	0.40	3.19 ± 0.28	--	--
Carbon	MMD-05	Andes mts., Peru	2013-08-12	-12.889	-71.355	sed.	258	188	1.37	--	3.30 ± 0.22	--
Madre de Dios	MMD-28	Foreland-floodplain, Peru	2013-08-16	-12.580	-70.096	sed.	107	128	0.84	--	3.24 ± 0.22	0.82 ± 0.15
Madre de Dios	MMD-32	Puerto Maldonado, Peru	2013-08-18	-12.563	-69.176	sed.	147	163	0.90	--	3.72 ± 0.22	1.08 ± 0.15
Inambari	MMD-29	Puerto Maldonado, Peru	2013-08-16	-12.719	-69.752	mixed	211	160	1.32	--	3.17 ± 0.22	0.74 ± 0.15
Piedras	MMD-34	Puerto Maldonado, Peru	2013-08-19	-12.519	-69.248	sed.	113	393	0.29	--	4.72 ± 0.22	1.53 ± 0.15
Solimões (Jun 2005)	AM-05-(05-08)	Manacapuru, Brazil	2005-06-04	-3.325	-60.549	sed.	106	158	0.67	2.43 ± 0.09	--	--
Solimões (Dec 2014)	AM14-36	Manacapuru, Brazil	2014-12-10	-3.317	-60.550	sed.	134	155	0.87	2.01 ± 0.24	--	1.02 ± 0.15
Negro	AM14-40	Manaus, Brazil	2014-12-11	-3.167	-60.004	sed.	70	90	0.78	2.00 ± 0.28	--	0.56 ± 0.15
Madeira	AM06-(34-43)	Foz Madeira, Brazil	2006-03-19	-3.408	-58.791	sed.	146	153	0.95	2.50 ± 0.09	--	--
Amazon	AM06-(23-30)	Iracema, Brazil	2006-03-18	-3.318	-58.828	sed.	119	145	0.82	2.54 ± 0.09	--	0.88 ± 0.15

All samples were taken at the surface (0m), with the following exceptions: AM-05-(05-08) composite of 0-21m; AM06-(23-30) composite of 0-45m (two depth profiles); AM06-(34-43) composite of 0-15m; AN-14-(42-44) composite of surf. samples taken at Duclas and at the mouth; CAN-10-(03+05) composite of 2.5 and 8.5m; CAN-10-(11+14) composite of 5 and 19.4m; CAN-10-(46+48) composite of 1.5 and 4.8m.

* Affected by anthropogenic activity. The Mississippi, Hondo, and Los Angeles rivers are incorporate significant industrial and urban runoff. Changjiang chemistry is affected by extensive irrigation and farming of rice paddies in the floodplain (Ding et al., 2004). Lower Kern river was sampled downstream of a dam reservoir in which water chemistry is strongly modified by diatom growth (Baronas et al., 2017a).

** Dominant lithology. bas. = basaltic; gran. = granitic; sed. = sedimentary.

Previous work has shown how the hydrodynamic sorting of sediments in large rivers can result in variations of the elemental (Bouchez et al., 2011) and Li isotope composition of sediments with depth (Dellinger et al., 2014). In deep and wide river channels, the flow velocity and turbulence are lower, allowing larger and denser grains (in many cases quartz and other primary minerals) to preferentially settle into bedload, while smaller clay grains remain suspended (e.g., Bouchez et al., 2011). If there is chemical difference between the fine and the coarse sediments, this can be observed in large river depth profiles. Here we show that hydrodynamic sorting of sediments also affects the $\delta^{30}\text{Si}$ and Ge/Si composition of samples in the Andes-Amazon system (Fig. 3). At high elevations, the bedload composition of shallow, turbulent streams is indistinguishable from the shale-dominated bedrock (Fig. 3a-c). However, with decreasing elevation along the Andes-Amazon transect, the riverine bedload $\delta^{30}\text{Si}$ increases and Ge/Si decreases (Fig. 3a,b) - the opposite from an expected weathering signal but expected if hydrodynamic sorting is affecting the bedload composition. Quartz, although not measured in this location, typically has the lowest Ge/Si ratios of all silicate minerals (Mortlock & Froelich, 1987; Kurtz et al., 2002) and higher $\delta^{30}\text{Si}$ relative to fine sediments (Bayon et al., 2018) and becomes progressively enriched in the river bedload relative to the suspended load during downstream transport (Bouchez et al., 2011), explaining the distinctive trend with elevation in Ge/Si and $\delta^{30}\text{Si}$ compositions.

The sediment depth profile in the Madre de Dios river is also expected to show a gradient in $\delta^{30}\text{Si}$ due to sorting, with lower $\delta^{30}\text{Si}$ near the surface (due to dominance of clay phases) and higher values at depth. The observed trend (Fig. 3d) is consistent with this interpretation, although it must be noted that the trend is small relative to the analytical uncertainty. Nevertheless, a similar sorting effect is seen in Ge/Si signatures further downstream after the Madre de Dios joins other Andean tributaries to become the Madeira River (Fig. 3e, Appendix Table B1). This observation is again consistent with a hydrodynamic separation of clays (high Ge/Si) from heavier igneous minerals (low Ge/Si) (Table 2). However, it is difficult to tell whether the clays carried in suspended load are secondary weathering products formed within the watershed, or derived primarily from the Andean shales (Dellinger et al., 2014) and concentrated near the surface due to sorting.

In contrast to $\delta^{30}\text{Si}$ and Ge/Si, the downstream sorting effect is not reflected in $\delta^{74}\text{Ge}$ values of the bedloads in the Andes-Amazon (Fig. 3c), which implies that quartz and other heavier minerals have $\delta^{74}\text{Ge}$ values similar to the clay-rich suspended load or that these phases add little Ge. Although we lack depth profile data for $\delta^{74}\text{Ge}$, the observation from bedload-elevation trend is again consistent with limited Ge isotope fractionation observed in solid samples and the very limited range of $\delta^{74}\text{Ge}$ in various silicate rocks, despite variations in Ge/Si (Rouxel et al., 2006).

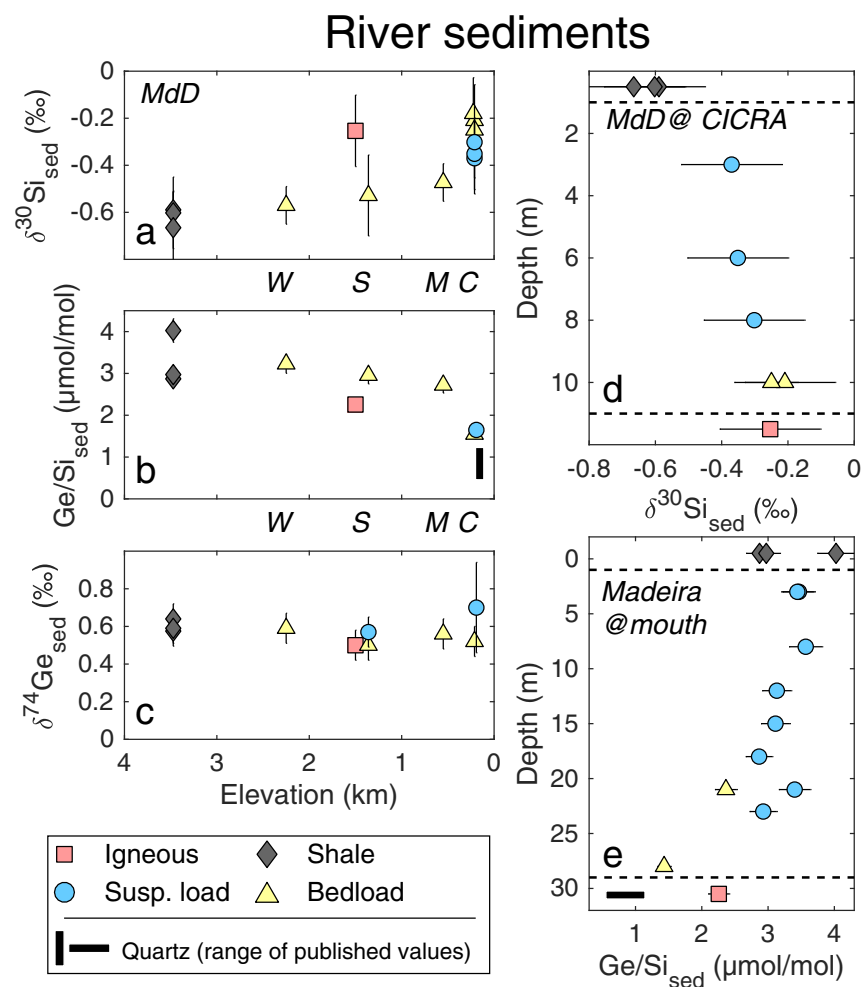


Figure 3: Effects of sediment sorting on $\delta^{74}\text{Ge}$, $\delta^{30}\text{Si}$, and Ge/Si of solids in the Andes-Amazon. a) $\delta^{30}\text{Si}$, b) Ge/Si , and c) $\delta^{74}\text{Ge}$ relationship with elevation in the Andes-Amazon transect in Madre de Dios watershed (Table 2). Site naming convention retained from Torres et al. (2015) and Torres et al. (2016) (the latter in parentheses): W = Kosñipata Riv. at Wayqecha (Mountain-1); S = Kosñipata Riv. at Sen Pedro (Mountain-2); M = Alto Madre de Dios Riv. at MLC (Mountain-front); C = Madre de Dios Riv. at CICRA (Foreland-floodplain). d) $\delta^{30}\text{Si}$ and e) Ge/Si composition of suspended sediment as a function of depth in the Amazon floodplain. Also shown is the composition of Andean shales (top) and igneous rocks (bottom) (Table 2). The black rectangle in panels b and e shows the range of previously measured quartz separates (Murnane & Stallard, 1990; Kurtz et al., 2002).

Table 2: Ge and Si concentrations and isotope compositions of rocks and river sediments. Different digestion methods are described in detail in Appendix A; fus. = fusion, ash. = ashing. For Peru locations, see Torres et al. (2015).

Sample	Sample ID	Location	Elevation, m	Digestion method (Ge)	Ge, $\mu\text{g/g}$	$\delta^{74}\text{Ge}$, ‰	Digestion method (Si)	Si, g/g	$\delta^{30}\text{Si}$, ‰	Ge/Si, $\mu\text{mol/mol}$
<i>Andean rocks</i>										
Igneous	WP-13	San Pedro, Peru	~1500	HF	2.16	0.46 ± 0.23	NaOH fus.	0.373	-0.25 ± 0.15	2.26
				HNO ₃ +HF	2.19	0.54 ± 0.08				
Shale	ROCK-1	Wayqecha, Peru	3472	HF	1.96	0.66 ± 0.23	NaOH fus.	0.243	-0.62 ± 0.15	2.86
				HNO ₃ +HF	1.81	0.62 ± 0.08	ash. + NaOH fus.	0.266	-0.56 ± 0.16	2.63
Shale	ROCK-2	Wayqecha, Peru	3472	HF	1.99	0.61 ± 0.23	NaOH fus.	0.259	-0.60 ± 0.15	2.91
				HNO ₃ +HF	1.90	0.54 ± 0.08				
Shale	ROCK-4	Wayqecha, Peru	3472	HF	2.64	0.58 ± 0.23	NaOH fus.	0.254	-0.67 ± 0.15	4.01
				HNO ₃ +HF	2.63	0.60 ± 0.08				
<i>Andes-Amazon river loads</i>										
Kosñipata bedload	R2250_21_03	Wayqecha, Peru	2250	HNO ₃ +HF	2.26	0.59 ± 0.08	NaOH fus.	0.258	-0.55 ± 0.15	3.23
							ash. + NaOH fus.	0.285	-0.59 ± 0.15	
Kosñipata susp. load	KOS15	San Pedro, Peru	1360	HF	2.04	0.57 ± 0.08	--	--	--	--
Kosñipata bedload	S200511	San Pedro, Peru	1360	HNO ₃ +HF	2.17	0.50 ± 0.08	NaOH fus.	0.284	-0.53 ± 0.17	2.96
Alto Madre de Dios bedload	RKOS-0550	MLC, Peru	550	HNO ₃ +HF	2.05	0.56 ± 0.08	NaOH fus.	0.284	-0.48 ± 0.15	2.79
							ash. + NaOH fus.	0.298	-0.47 ± 0.15	
Madre de Dios susp. load	CMD-29_3m	CICRA, Peru	212	--	--	--	NaOH fus.	0.324	-0.37 ± 0.15	--
Madre de Dios susp. load	CMD-29_6m	CICRA, Peru	212	--	--	--	NaOH fus.	0.344	-0.35 ± 0.15	--
Madre de Dios susp. load	CMD-29_8m	CICRA, Peru	212	--	--	--	NaOH fus.	0.313	-0.30 ± 0.15	--
Madre de Dios bedload	CMD-29_10m	CICRA, Peru	212	--	--	--	NaOH fus.	0.313	-0.21 ± 0.15	--
Madre de Dios bedload	RPtMA-0177	CICRA, Peru	212	HNO ₃ +HF	1.50	0.52 ± 0.08	NaOH fus.	0.368	-0.24 ± 0.15	1.55
							NaOH fus.	0.380	-0.26 ± 0.15	
Colorado bedload	RCOL_0240	Boca Colorado, Peru	240	--	--	--	NaOH fus.	0.309	-0.22 ± 0.15	--
Amigos bedload	RAMI_0225	CICRA, Peru	225	--	--	--	NaOH fus.	0.317	-0.18 ± 0.15	--
Torre susp. load	RT15	Tambopata, Peru	192	HF	1.74	0.70 ± 0.24	HF	0.408	--	1.65
<i>Other</i>										
Watson susp. load	JO-14	Kangerlussuaq, Greenland	--	HF	1.09	0.48 ± 0.23	HF	0.355	--	1.18
Mekong susp. load	ME14	Luang Prabang, Laos	--	HF	2.00	0.49 ± 0.24	HF	0.349	--	2.21

3.2 Global riverine Ge isotope and Ge/Si composition

Dissolved riverine Ge is primarily derived from weathering of silicate rocks, whereas carbonate and evaporite minerals typically contain negligible amounts of Ge (Burton et al., 1959). Rivers draining industrialized areas have been shown to exhibit elevated Ge concentrations, most often due to contamination via Ge-rich coal and fly-ash (Froelich et al., 1992). The dataset presented in this study includes various rivers from around the globe, with a focus on relatively pristine catchments. The riverine dissolved Ge isotope composition ($\delta^{74}\text{Ge}_{\text{riv}}$) ranges from 0.86 ± 0.24 to 5.20 ± 0.24 ‰ ($n = 40$), with a standard deviation of 1.02 ‰ (Table 1, Figs 1b and 4), expanding the previously reported range (Baronas et al., 2017a). All rivers measured to date are isotopically heavier than the silicate rocks from which the dissolved Ge is sourced ($\delta^{74}\text{Ge}_{\text{rock}} = 0.4 - 0.8$ ‰; Rouxel & Luais (2017)). Consistent with the previous smaller dataset of Baronas et al. (2017a), there is no identifiable relationship between riverine $\delta^{74}\text{Ge}$ composition and the dominant watershed lithology (Table 1, Fig. 4), major element proxies (e.g., Ca/Na; not shown, data given in Appendix Table B2), or degree of anthropogenic contamination.

Using the signatures of the major rivers in this dataset (Amazon, Changjiang, Mackenzie, Mekong, and Fraser), the flux-weighted global $\delta^{74}\text{Ge}_{\text{riv}}$ value can be estimated, using the mean river discharge as reported by Milliman & Farnsworth (2011). On this basis, the mean Ge flux-weighted $\delta^{74}\text{Ge}_{\text{riv}}$ value is calculated to be 2.62 ± 0.16 ‰ (flux-weighted uncertainty, including 10% error on water discharge and analytical errors of Ge and $\delta^{74}\text{Ge}$ measurements), significantly lower than the previous preliminary estimate of 3.5 ± 1.5 ‰ (Baronas et al., 2017a). The Mississippi, Changjiang, and Mekong rivers included here are known to be significantly affected by hydrothermal or anthropogenic inputs (Baronas et al., 2016; Han et al., 2015). Excluding these rivers has no effect on global $\delta^{74}\text{Ge}_{\text{riv}}$ (2.56 ± 0.15 ‰) but strongly impacts Ge/Si_{riv} which is reduced from 0.90 ± 0.06 $\mu\text{mol/mol}$ to 0.68 ± 0.05 $\mu\text{mol/mol}$, bringing it to closer agreement with the previous estimate of 0.54 $\mu\text{mol/mol}$ that was primarily based on small pristine streams (Froelich et al., 1992).

The large rivers analyzed in this study represent ~24% of the global water discharge (Milliman & Farnsworth, 2011) and ~20-30% of the estimated riverine Ge flux to the ocean (there is uncertainty due to anthropogenic contamination). The Amazon River Ge flux (~0.7 Mmol/y) is higher than all the other rivers in this study combined (~0.5 Mmol/y) and therefore exerts a strong influence on the calculated flux-weighted composition. The Ge/Si of the Amazon river at Obidos has been measured to vary between 0.57 and 0.79 $\mu\text{mol/mol}$ ($n = 3$; see Appendix Table B3 and Gaillardet et al. (1999, 2014)). Measurements of the three major Amazon tributaries (Solimões, Madeira, and Negro) all show a remarkably narrow $\delta^{74}\text{Ge}$ range of 2.0-2.5 ‰ (Table 1). Furthermore, although only two data points are available, there does not appear to be a large seasonal $\delta^{74}\text{Ge}$ variation in the Solimões (2.0-2.4 ‰). We note that there is currently no $\delta^{74}\text{Ge}$ data available for two other major Amazon tributaries, the Tapajos and the Trombetas. Considering all of the above, we propose a conservative mean (pristine) discharge-weighted global $\delta^{74}\text{Ge}_{\text{riv}}$ of 2.6 ± 0.5 ‰, adopting the value calculated above, with a higher arbitrary uncertainty which is intermediate between the flux-weighted analytical uncertainty of large rivers (0.15 ‰, likely an underestimate) and standard deviation of all river samples measured to date (1.0 ‰, likely an overestimate). We expect that this value should encompass any potential inaccuracies due to as of yet unsampled rivers or unconstrained temporal variations in large rivers. For Ge/Si, the Froelich et al. (1992) estimate of 0.54 ± 0.10 $\mu\text{mol/mol}$ is retained. Time-series measurements of the Amazon and other major rivers of the world are needed to refine these values further.

3.3 Mechanisms controlling Ge and Si isotope composition of rivers

3.3.1 Controls on dissolved Ge composition of rivers

The ~ 5 ‰ range observed globally in dissolved $\delta^{74}\text{Ge}_{\text{riv}}$ composition is considerable, given the relatively small mass difference between ^{74}Ge and ^{70}Ge . As discussed above, such high apparent fractionation is consistent with the fact that only a few percent of Ge is exported in the dissolved phase during weathering (Gaillardet et al., 2014), making it more sensitive to isotopic fractionation in the dissolved load (Bouchez et al., 2013).

There is no observable relationship between $\delta^{74}\text{Ge}_{\text{riv}}$ and dissolved Ge concentration (Fig. 4a), which is not unexpected, given that Ge concentration can be influenced by a number of factors that do not affect $\delta^{74}\text{Ge}_{\text{riv}}$, such as dilution by rain water and concentration by evaporation. A more robust negative correlation is observed between dissolved riverine $\delta^{74}\text{Ge}$ and Ge/Si signatures (Fig. 4b). Ge/Si ratios are primarily fractionated by the formation of secondary weathering products, such as refractory oxides and aluminosilicate clays (Mortlock & Froelich, 1987; Kurtz et al., 2002) and the same process appears very likely to be responsible for $\delta^{74}\text{Ge}_{\text{riv}}$ fractionation as well.

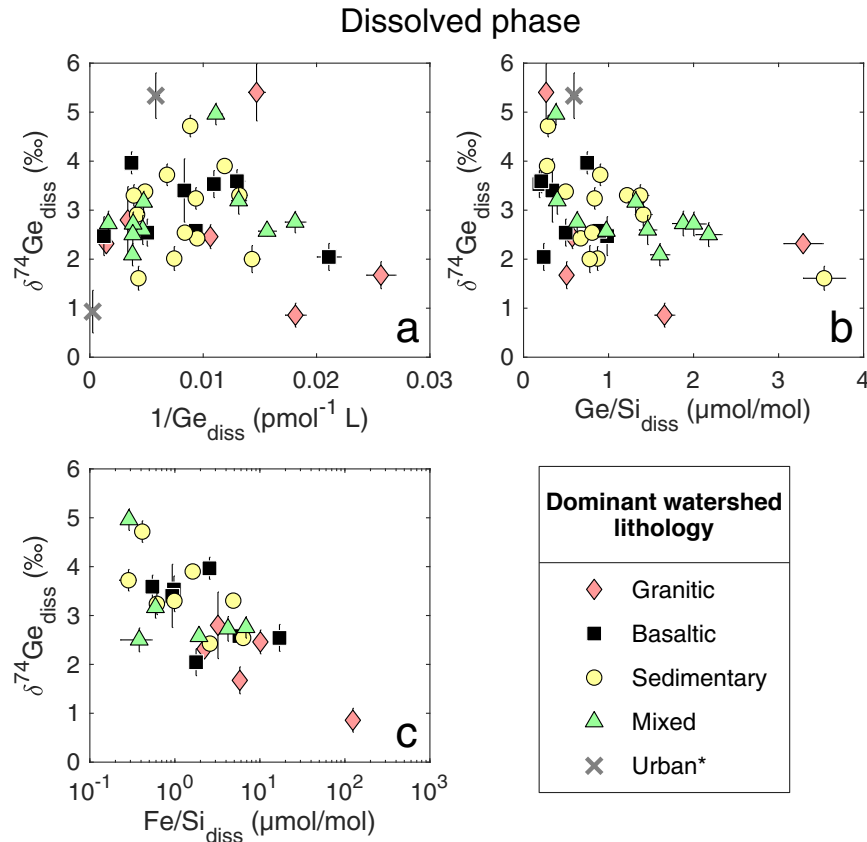


Figure 4: Dissolved $\delta^{74}\text{Ge}$ composition in rivers draining various lithologies (as designated in Table 1). a) $\delta^{74}\text{Ge}$ as a function of Ge concentration reciprocal. b) $\delta^{74}\text{Ge}$ as a function of Ge/Si ratio. c) $\delta^{74}\text{Ge}$ as a function of Fe/Si ratio.

*Small rivers draining primarily urban areas and with largely paved riverbeds. The Los Angeles river is not shown due to its very high Ge/Si (25.9 $\mu\text{mol/mol}$).

The good correlation between $\delta^{74}\text{Ge}_{\text{riv}}$ and dissolved Fe/Si (Fig. 4c) provides further indication of the important role that iron might play in Ge isotope dynamics. The siderophilic character of Ge is well documented (Bernstein & Waychunas, 1987; Mortlock & Froelich, 1987; Pokrovsky et al., 2006), including isotopic fractionation of Ge during adsorption and co-precipitation with Fe oxides (Pokrovsky et al., 2014). It is therefore likely that iron oxides in particular strongly affect $\delta^{74}\text{Ge}_{\text{riv}}$ signatures.

Finally, it is possible that riverine $\delta^{74}\text{Ge}$ is also fractionated by Ge association with organic complexes, such as humic acids (Pokrovski & Schott, 1998), potentially explaining the correlation with dissolved Fe, as the latter is well known to associate with organic compounds (e.g., Allard et al., 2004). However, this is unlikely to provide a systematic explanation for observed compositions, given the similarity in $\delta^{74}\text{Ge}$ between the DOC-rich Negro River and the DOC-poor Solimões or Madeira (Table 1).

3.3.2 Isotopic fractionation of Ge and Si during secondary weathering processes

Due to precipitation, adsorption, and/or biological uptake, only a fraction of a given element (X) initially released during the dissolution of primary minerals may remain in solution. Previous studies have shown that this fraction, often referred to as $f_{\text{diss}}^{\text{X}}$, where X is the element of interest, can be estimated utilizing a conservative solute that is not significantly incorporated into secondary mineral phases (or taken up by plants), for example, Na (Gislason et al., 1996):

$$f_{\text{diss}}^{\text{X}} = \frac{(\text{X/Na})_{\text{diss}}}{(\text{X/Na})_{\text{rock}}} \quad (1)$$

where subscript *rock* refers to the elemental ratio associated with solute release via primary mineral dissolution, which can often be approximated by analyzing river-transported sediments or using the composition of the Upper Continental Crust (UCC), if river sediment data is unavailable. For accurate $f_{\text{diss}}^{\text{X}}$ estimates, dissolved Na concentrations need to be corrected for cyclic salt (rain and evaporite) inputs.

Given that silicate rocks have a limited range of Ge/Si, $\delta^{74}\text{Ge}$, and $\delta^{30}\text{Si}$ compositions (Rouxel & Luais, 2017; Frings et al., 2016), the initial dissolution of their constituent minerals during weathering should result in negligible elemental or isotopic fractionation. The variations in dissolved riverine composition should then depend primarily on the degree of removal from solution ($f_{\text{diss}}^{\text{X}}$) and the fractionation factor (α) associated with this removal. Assuming the catchment behaves like a steady state flow-through reactor ("batch" model) (Georg et al., 2006a; Bouchez et al., 2013) yields a linear functional relationship between the elemental or isotopic ratio R and f_{diss} :

$$R_{\text{diss}} = \frac{R_{\text{rock}}}{\alpha + f_{\text{diss}}^{\text{X}}(1 - \alpha)} \quad (2)$$

where α is the fractionation factor (often referred to as the partitioning coefficient in the case of elemental fractionation). In cases where the exchange between the dissolving and precipitating phases is limited, the solution composition may be better described by a Rayleigh equation (Rayleigh, 1902), resulting in a power-law relationship between R and f_{diss} :

$$R_{\text{diss}} = R_{\text{rock}}(f_{\text{diss}}^{\text{X}})^{\alpha-1} \quad (3)$$

Applying either Eq. 2 or 3 to measurements of river waters assumes that the riverine composition represents a single flowpath of the evolved weathering fluid, and can therefore be represented by a single f_{diss}^X value. Due to the non-linearity of these relationships, this assumption can lead to spurious results if fluids that have undergone variable extents of reaction (and associated isotopic fractionation) are mixed. To account for the effects of mixing, Druhan & Maher (2017) have proposed a revised Rayleigh model that takes into account the mixing of variable water transit times, therefore offering a more realistic representation of the catchment hydrology. As shown by Druhan & Maher (2017), the use of an exponential water transit time distribution results in a relationship between R_{diss} and f_{diss} that is identical to Eq. 2. Equation 2 is derived from a simple mass-balanced chemical fractionation between any two phases (Appendix C1) and was initially applied to elemental mantle-crust differentiation (Hofmann, 1988). From here on we therefore refer to this model as the "mixed open system" model, to acknowledge that both an exponential fluid transit time distribution and open system isotopic exchange between fluids and solids yield the same relationship between R_{diss} and f_{diss} . We note that the exact water transit time distribution in rivers is currently unconstrained. The shape of this distribution in different rivers and its effect on solute isotope signatures requires additional work that is outside the scope of this study.

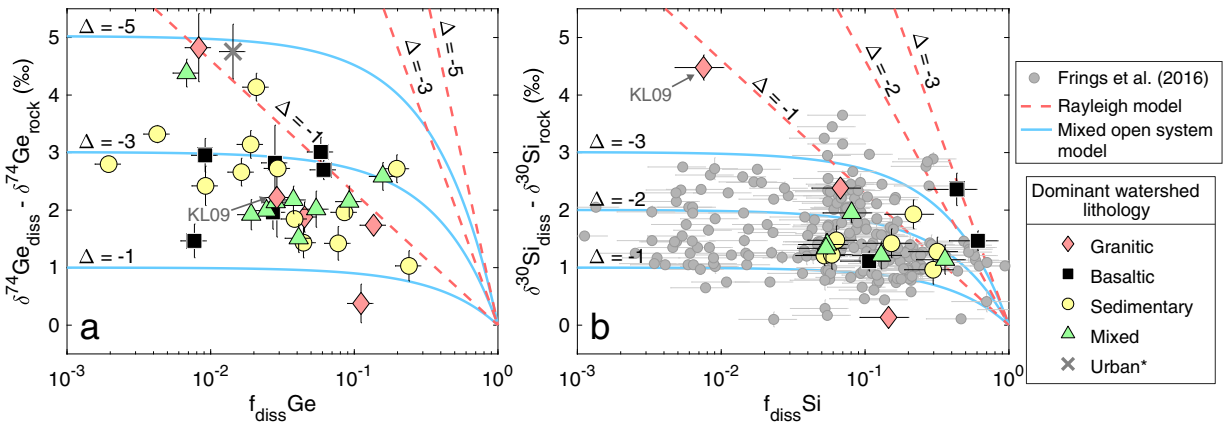


Figure 5: Dissolved $\delta^{74}\text{Ge}$ (a) and $\delta^{30}\text{Si}$ (b) composition in rivers as a function of $f_{\text{diss}}^{\text{Ge}}$ and $f_{\text{diss}}^{\text{Si}}$, respectively, i.e., the fraction of each element remaining in solution after uptake by secondary weathering phases and biota (see Eq. 1). Lines show theoretical fluid composition evolution with a range of isotope fractionation factors ($\Delta_{\text{solid-diss}}$) for both models discussed in text (see Section 3.4.1).

*Small rivers draining primarily urban areas and with largely paved riverbeds.

The relationship between the isotopic composition of Si and Ge and the fraction of each element remaining in solution is shown in Fig. 5. The individual $f_{\text{diss}}^{\text{Ge}}$ and $f_{\text{diss}}^{\text{Si}}$ values for the rivers presented here are given in Appendix Table C1. There are three main take-aways from this compilation. First, both in the case of $\delta^{74}\text{Ge}_{\text{diss}}$ and $\delta^{30}\text{Si}_{\text{diss}}$, the majority of the data is best explained by the mixed open system model, whereas the Rayleigh model predicts heavier isotopic composition than observed, even for relatively low fractionation factors (Fig. 5). This is not surprising, considering the complex hydrological structure of catchments which results in both continuous chemical interaction of fluids with the rocks (open system behavior) and mixing of fluids with variable transit times (Druhan & Maher, 2017). The one clear exception that requires

a Rayleigh model is the Lower Kern River (KL09) $\delta^{30}\text{Si}_{\text{diss}}$ composition (Fig. 5b). This strong fractionation is caused by diatom drawdown of Si in a dam reservoir, which we discuss in Section 3.4.

Second, $f_{\text{diss}}^{\text{Ge}}$ values are generally about an order of magnitude lower than most $f_{\text{diss}}^{\text{Si}}$ values, although the latter do span a wide range (Fig. 5, Table C1). This difference is consistent with the contrasting $\delta^{74}\text{Ge}$ and $\delta^{30}\text{Si}$ behavior in weathered river sediments, as discussed in Section 3.1.

Finally, the relationships of $f_{\text{diss}}^{\text{Ge}}$ vs $\delta^{74}\text{Ge}_{\text{diss}}$ and $f_{\text{diss}}^{\text{Si}}$ vs $\delta^{30}\text{Si}_{\text{diss}}$ are both weak. This is likely because mixed open system behavior reduces the variability in δ_{diss} at low f_{diss} values (i.e. in Fig. 5 the solid lines plateau at low f_{diss} values in log-space). Nevertheless, significant scatter is observed in both $\delta^{74}\text{Ge}_{\text{diss}}$ and $\delta^{30}\text{Si}_{\text{diss}}$ at any given f_{diss} value, suggesting that substantial isotopic variability of these solutes is caused by other factors, such as 1) variable reaction products, mechanisms, and rates, resulting in different isotope fractionation factors (Pokrovsky et al., 2014; Frings et al., 2016); 2) variable water transit time distributions (Druhan & Maher, 2017); 3) other isotope fractionation mechanisms not reflected in this simple model, e.g., element cycling by vegetation or other biota; or 4) any combination of the above. Additional insights are required in order ascertain the relative roles of these processes on isotopic ratios.

3.4 Ge/Si-isotope multi-proxy: biological vs. secondary fractionation

It has been previously demonstrated that the coupled use of $\delta^{30}\text{Si}$ and Ge/Si can qualitatively deconvolve biological fractionation from that associated with secondary mineral precipitation, since Ge/Si is fractionated in the opposite sense by plants (depleted Ge/Si) relative to secondary minerals (enriched Ge/Si), while $\delta^{30}\text{Si}$ becomes depleted during both of these processes (e.g., Cornelis et al., 2011). This dual-proxy approach can also be applied on a global scale by comparing the $\delta^{30}\text{Si}$ and Ge/Si signatures in rivers. Although global compilations of both $\delta^{30}\text{Si}$ (Frings et al., 2016) and Ge/Si (Froelich et al., 1992) exist, they rely on separate sets of samples, and the potentially large (or poorly constrained) temporal-variability of these signatures has until now complicated the robust comparison of these proxies in riverine signatures on a global scale. As discussed above, each river represents a mixture of subsurface flowpaths and the dashed trends in Fig. 6 can therefore be conceptualized as an expression of variable intra-catchment mixing between two universal end-members (unfractionated and strongly fractionated fluids), or more realistically a continuous probability distribution of fluid compositions. Importantly, the negative correlation between riverine $\delta^{30}\text{Si}_{\text{diss}}$ and $\text{Ge/Si}_{\text{diss}}$ (Fig. 6a) demonstrates that to a first-order these signatures are controlled by secondary mineral precipitation, with notable exceptions where strong biological fractionation is observed. In contrast, biofractionation (as suggested by the offset along a positive slope in Fig. 6a) appears to have little effect on $\delta^{74}\text{Ge}_{\text{diss}}$ (no slope in Fig. 6b).

While the qualitative observations provided above are useful, ultimately, the complexity of natural systems means that the isotopic data of a single solute is often insufficient to quantitatively reconstruct the combination of processes that have taken place to impart that signature. However, the combination of proxies can, in certain cases, be used to deconvolve the dominant first order effects controlling isotopic signatures. Below, we propose a model that utilizes the combination of riverine Si and Ge concentrations and isotopic signatures to 1) constrain biological vs. secondary phase uptake of Si and Ge; and 2) refine the empirical estimates of biological and secondary phase isotope fractionation factors of Si and Ge.

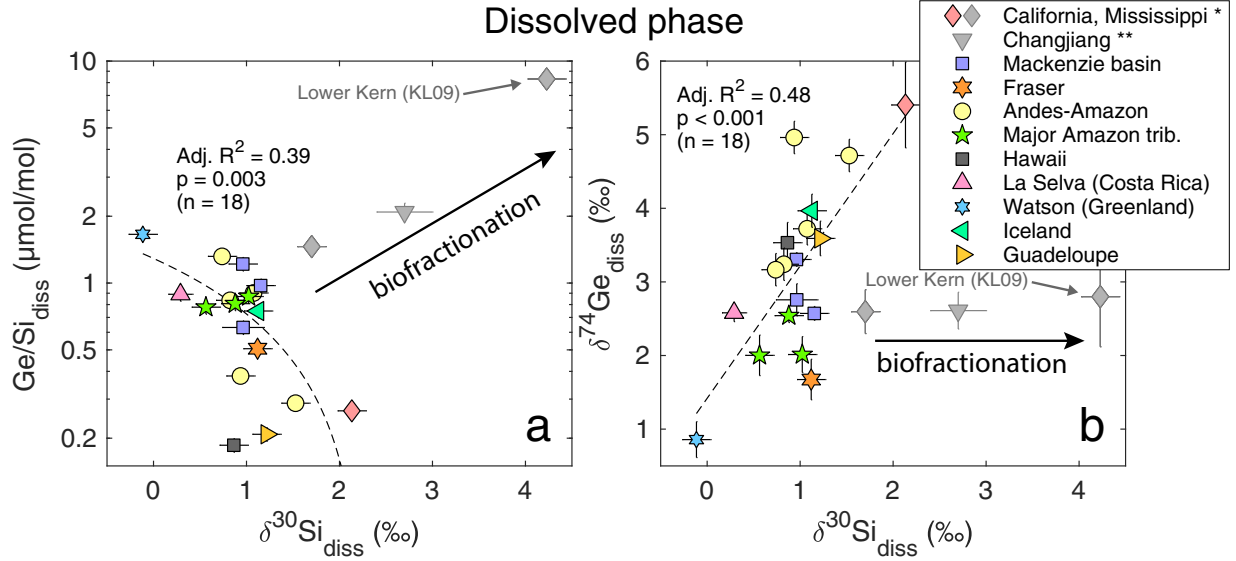


Figure 6: Relationship of dissolved $\delta^{30}\text{Si}$ with Ge/Si (a) and with $\delta^{74}\text{Ge}$ (b) in global rivers. Note the log scale of y-axis in panel a. Statistical parameters refer to the linear regression fit (dashed line). The gray points are samples affected by biological fractionation or anthropogenic disturbance and are not used in the regression: *The Mississippi and Lower Kern rivers, as discussed above; **The Changjiang river, affected by extensive rice paddy agriculture in the floodplain. For the Changjiang, the plotted $\delta^{30}\text{Si}$ and error bars show the range of values determined by Ding et al. (2004), Ge/Si and $\delta^{74}\text{Ge}$ data from this study (Table 1).

3.4.1 Ge/Si-isotope fractionation model: description

Within the mixed open system (Eq. 2), the distribution of elemental or isotopic ratios between multiple phases i can be described by a simple mass balance:

$$R_{\text{rock}} = \sum R_i f_i^X = R_{\text{sec}} f_{\text{sec}}^X + R_{\text{bio}} f_{\text{bio}}^X + R_{\text{diss}} f_{\text{diss}}^X \quad (4)$$

where f^X is the molar fraction of species X in the denominator of ratio R. Equation 4 represents the uptake of a portion of Si and Ge in secondary mineral and biological phases (subscripts *sec* and *bio*, respectively). The equivalence of Eqs 2 and 4 in both two and three end-member cases is demonstrated in Appendix C1.

The individual fractionation factors associated with each process are defined as:

$$\alpha_{\text{sec}}^R = \frac{R_{\text{sec}}}{R_{\text{diss}}} \quad (5)$$

$$\alpha_{\text{bio}}^R = \frac{R_{\text{bio}}}{R_{\text{diss}}} \quad (6)$$

Finally, maintaining mass balance requires that

$$f_{\text{sec}} + f_{\text{bio}} + f_{\text{diss}} = 1 \quad (7)$$

Applying Eqs. 4-7 to Ge/Si fractionation ($R = \text{Ge/Si}$, $X = \text{Si}$) and rearranging yields:

$$f_{\text{sec}}^{\text{Si}} = \frac{\frac{\text{Ge/Si}_{\text{rock}}}{\text{Ge/Si}_{\text{diss}}} - f_{\text{diss}}^{\text{Si}} (1 - \alpha_{\text{bio}}^{\text{Ge/Si}}) - \alpha_{\text{bio}}^{\text{Ge/Si}}}{\alpha_{\text{sec}}^{\text{Ge/Si}} - \alpha_{\text{bio}}^{\text{Ge/Si}}} \quad (8)$$

As discussed in Section 3.1, river sediment Ge/Si and Si/Na ratios can be affected by dilution with Ge- and Na-poor quartz, especially in the bedload (Fig. 3), which can bias the $f_{\text{diss}}^{\text{Si}}$ and $f_{\text{diss}}^{\text{Ge}}$ estimates. To minimize this possibility, we calculate the fraction of Si remaining in solution as:

$$f_{\text{diss}}^{\text{Si}} = \text{Si/Na}_{\text{diss}} \frac{\text{Ge/Si}_{\text{rock}}}{\text{Ge/Na}_{\text{sed}}} \quad (9)$$

where $\text{Ge/Na}_{\text{sed}}$ is the ratio measured in river sediments and $\text{Ge/Si}_{\text{rock}}$ is the ratio of weathering silicates. In the absence of robust constraints (e.g. suspended sediment depth profiles) $\text{Ge/Si}_{\text{rock}}$ was taken to be intermediate between the UCC and acidic quartz-free rocks ($\text{Ge/Si}_{\text{rock}}$ values used for each modeled sample are given in Appendix Table C1). This approach assumes that river bedload $\text{Ge/Na}_{\text{sed}}$ is a good approximation of primary $\text{Ge/Na}_{\text{rock}}$, which may not be exactly true. Nevertheless, it results in a more robust estimate of $f_{\text{diss}}^{\text{Si}}$ because Ge/Na is much less affected by the quartz content of the rocks or sediments than Si/Na (compare UCC and average acidic rock values in Table C1).

Partitioning coefficients $\alpha_{\text{sec}}^{\text{Ge/Si}}$ and $\alpha_{\text{bio}}^{\text{Ge/Si}}$ have been determined by previous workers in a number of settings (often referred to as K_d or K_w) and generally are in the range of 1.2-3 for $\alpha_{\text{sec}}^{\text{Ge/Si}}$ (Murnane & Stallard, 1990; Froelich et al., 1992) and 0.005-0.56 for $\alpha_{\text{bio}}^{\text{Ge/Si}}$ (Derry et al., 2005; Blecker et al., 2007; Meek et al., 2016). These ranges were used to calculate a range of $f_{\text{sec}}^{\text{Si}}$ and $f_{\text{bio}}^{\text{Si}}$ for the rivers presented here, with a few exceptions (Table C1; see Appendix C1 for details).

The mass partitioning of Ge between the three phases can be simply obtained from:

$$\text{Ge/Si}_i = \text{Ge/Si}_{\text{rock}} \frac{f_i^{\text{Ge}}}{f_i^{\text{Si}}} \quad (10)$$

where $i = \text{diss}, \text{sec}, \text{or } \text{bio}$. Using known Ge/Si partition coefficients (Eqs. 5-6), Eq. 10 allows the calculation of $f_{\text{sec}}^{\text{Ge}}$ and $f_{\text{bio}}^{\text{Ge}}$.

Eq. 4 can then be applied to Si and Ge isotope ratios, calculating $R_{\text{diss}}^{30/28}$ and $R_{\text{diss}}^{74/70}$ (see Appendix C1 for an explicit expression). This is done by assigning random values to the respective α_{sec} and α_{bio} factors and other input parameters from within the range determined in previous studies (Table C2). The $\alpha^{30/28}$ (often approximated as $\Delta^{30}\text{Si}$ in ‰ notation) values are summarized in Frings et al. (2016) and were conservatively assigned as -3 to 0 ‰ for both $\Delta^{30}\text{Si}_{\text{sec}}$ and $\Delta^{30}\text{Si}_{\text{bio}}$. There are very few previous estimates of possible $\Delta^{74}\text{Ge}_{\text{sec}}$ values and no estimates of $\Delta^{74}\text{Ge}_{\text{bio}}$. Therefore, a very conservative range of -6 to +6 ‰ has been applied to each.

The calculated $R_{\text{diss}}^{30/28}$ and $R_{\text{diss}}^{74/70}$ ratios are then compared to the measured values (Table 1). If either of the calculated values is outside of the 2 S.D. analytical uncertainty of the measured value, the whole set of calculations is discarded. The process is repeated 1 million times (i.e., a Monte Carlo approach), retaining only those runs where measured and calculated values agreed within the 2 S.D. analytical tolerance. This approach is immune to auto-correlation effects between variables and allows us to assess the full uncertainty of modeling results given the wide possible range of some input parameter values.

3.4.2 Ge/Si-isotope fractionation model: results and discussion

The detailed modeling results are summarized in Appendix Table C3. Excluding the dammed Lower Kern river sample KL09 (see discussion below), the calculated fraction of Si taken up by secondary weathering phases ($f_{\text{sec}}^{\text{Si}}$) in the sampled rivers ranges from (median $\pm 1\sigma$) $19 \pm 14\%$ to $79 \pm 11\%$ (avg. 54%) and the fraction of Si taken up biologically ($f_{\text{bio}}^{\text{Si}}$) ranges from $12 \pm 11\%$ to $54 \pm 19\%$ (avg. 32%). In contrast, Ge uptake was strongly dominated by secondary phases, with very little biological uptake: $f_{\text{sec}}^{\text{Ge}}$ between 79-98% (avg. 92%) and $f_{\text{bio}}^{\text{Ge}}$ between 1-6% (avg. 3%).

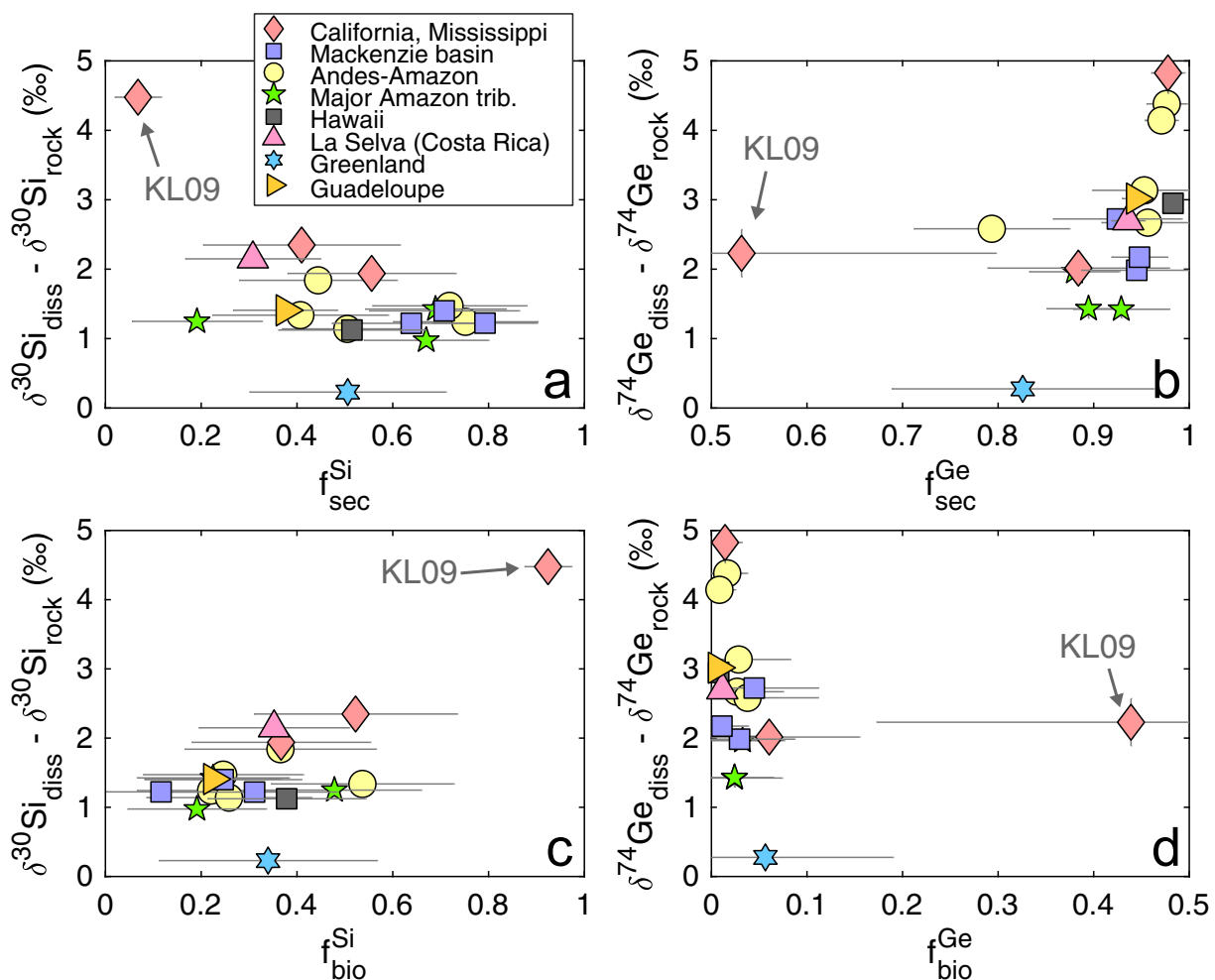


Figure 7: The relationship between the degree of measured apparent isotopic fractionation of dissolved riverine Si and Ge composition and the degree of removal via secondary weathering (a-b) and biological uptake (c-d), as modeled using dissolved Ge/Si composition (see Section 3.4 for model discussion). Lower Kern River sample (KL09) was taken downstream of a dam reservoir and shows an extreme degree of biological Si and Ge uptake by freshwater diatoms. KL09 is out of range in panel b. Symbols are plotted as medians and horizontal error bars as 1 standard deviation of the calculated range of values.

Again excluding sample KL09, neither $f_{\text{sec}}^{\text{Si}}$ nor $f_{\text{bio}}^{\text{Si}}$ shows a strong relationship with the apparent fractionation of riverine $\delta^{30}\text{Si}_{\text{diss}}$ (Fig. 7a,c; adj. $R^2 \approx 0$ in each case), suggesting that

both processes fractionate $\delta^{30}\text{Si}_{\text{diss}}$ to a similar degree. Apparent $\delta^{74}\text{Ge}_{\text{diss}}$ fractionation, on the other hand, shows a significant positive correlation with $f_{\text{sec}}^{\text{Ge}}$ (Fig. 7b; adj. $R^2 = 0.32$), suggesting that riverine $\delta^{74}\text{Ge}_{\text{diss}}$ signatures are primarily determined by fractionation during the formation of secondary weathering phases.

In cases where either $f_{\text{sec}}^{\text{X}}$ or $f_{\text{bio}}^{\text{X}}$ dominates the uptake of element X, the value of the fractionation factor $\Delta_{\text{sec}}^{\text{X}}$ or $\Delta_{\text{bio}}^{\text{X}}$, respectively, can be refined using the measured $\delta_{\text{diss}}^{\text{X}}$ value, using the approach described above (Eqs. 4-10 and Appendix C1). The detailed results are given in Appendix Table C3 and Figs. C4-C5. Excluding the glacial Watson River in West Greenland (discussed below), the calculated $\Delta^{74}\text{Ge}_{\text{sec}}$ ranges from -4.9 ± 0.4 to -1.6 ± 0.4 ‰ (median $\pm 1\sigma$), whereas $\Delta^{30}\text{Si}_{\text{sec}}$ ranges from -2.7 ± 0.4 to -1.1 ± 0.5 ‰. However, due to the fact that Si uptake is more evenly distributed between biological and secondary phases in most rivers, neither $\Delta^{30}\text{Si}_{\text{sec}}$ nor $\Delta^{30}\text{Si}_{\text{bio}}$ can be determined precisely (Fig. 8). Similarly, $\Delta^{74}\text{Ge}_{\text{bio}}$ cannot be determined precisely because only a very small fraction of Ge is usually taken up biologically, having little impact on $\delta^{74}\text{Ge}_{\text{diss}}$.

The one exception is Lower Kern River (KL09), where there is extensive biological uptake of Si and Ge by diatoms within a dam reservoir. Using the mixed open system ("batch") model results in an unrealistically large $\Delta^{30}\text{Si}_{\text{bio}}$ of -4.6 ± 0.3 ‰ (Table C3, Fig. C4). If instead a Rayleigh model (Eq. 3) is used for the biological uptake step, a $\Delta^{30}\text{Si}_{\text{bio}}$ of -2.1 ± 0.4 ‰ is calculated, in better agreement with previous studies of diatom $\delta^{30}\text{Si}$ fractionation (Frings et al., 2016). The biological uptake and fractionation of Ge isotopes in the Kern River dam reservoir can be modeled even more accurately by taking into account the difference in the composition of rivers entering and exiting the reservoir (Baronas et al., 2017a). Modeling the biological uptake of Ge as a Rayleigh process yields the only reliable estimate of $\Delta^{74}\text{Ge}_{\text{bio}}$ at -0.7 ± 0.7 ‰. This result suggests that $\delta^{74}\text{Ge}_{\text{diss}}$ is likely to be less affected by biological uptake, in agreement with the qualitative observations described above (Fig. 6b) and with marine diatom culture experiments (Rouxel & Luais, 2017).

The Watson River (JO-14) draining the Russel and Leverett glaciers in West Greenland also deserves a separate mention, given that the isotopic fractionation factors calculated for its watershed were significantly smaller compared with all other rivers ($\Delta^{30}\text{Si}_{\text{sec}}$ of -0.2 ± 0.3 ‰ and $\Delta^{74}\text{Ge}_{\text{sec}}$ of -0.3 ± 1.1 ‰; Fig. 8, Table C3). Lower $\delta^{30}\text{Si}_{\text{diss}}$ composition was previously observed in Icelandic glacial rivers (e.g., Georg et al., 2007). In contrast, $\delta^7\text{Li}_{\text{diss}}$ in glacial West Greenland rivers was strongly fractionated, most likely during Li uptake by Fe oxides derived from pyrite oxidation (Wimpenny et al., 2010). The isotopic fractionation of Mg (Wimpenny et al., 2011) and Fe (Stevenson et al., 2017) in Greenland appears to be primarily controlled by incongruent dissolution of primary minerals rather than the precipitation of secondary phases. Similar incongruency might affect riverine $\text{Ge}/\text{Si}_{\text{diss}}$, $\delta^{30}\text{Si}_{\text{diss}}$, and $\delta^{74}\text{Ge}_{\text{diss}}$ of the Watson River, potentially invalidating the modeling results here, given that the model assumes congruent dissolution of primary minerals. However, it is notable that using a global riverine clay dataset Bayon et al. (2018) have suggested limited $\delta^{30}\text{Si}$ fractionation in cold and arid environments, in agreement with our results from West Greenland. Overall, it appears that glacial weathering results in distinct geochemical and isotopic signatures in streams, and further research is needed to understand the mechanisms responsible.

With the exception of Greenland, the range of empirical $\Delta^{74}\text{Ge}_{\text{sec}}$ values determined here is consistent with previous experimental (Pokrovsky et al., 2014) and ab initio modeling (Li & Liu, 2010) studies of Ge removal by Fe oxide phases which determined $\Delta^{74}\text{Ge}_{\text{sec}} = -4.4$ to -1.7 ‰. Additional studies are needed to determine $\Delta^{74}\text{Ge}_{\text{sec}}$ associated with the formation of various aluminosilicate clays, but it is notable that the range of experimental Fe oxide $\Delta^{74}\text{Ge}_{\text{sec}}$ values

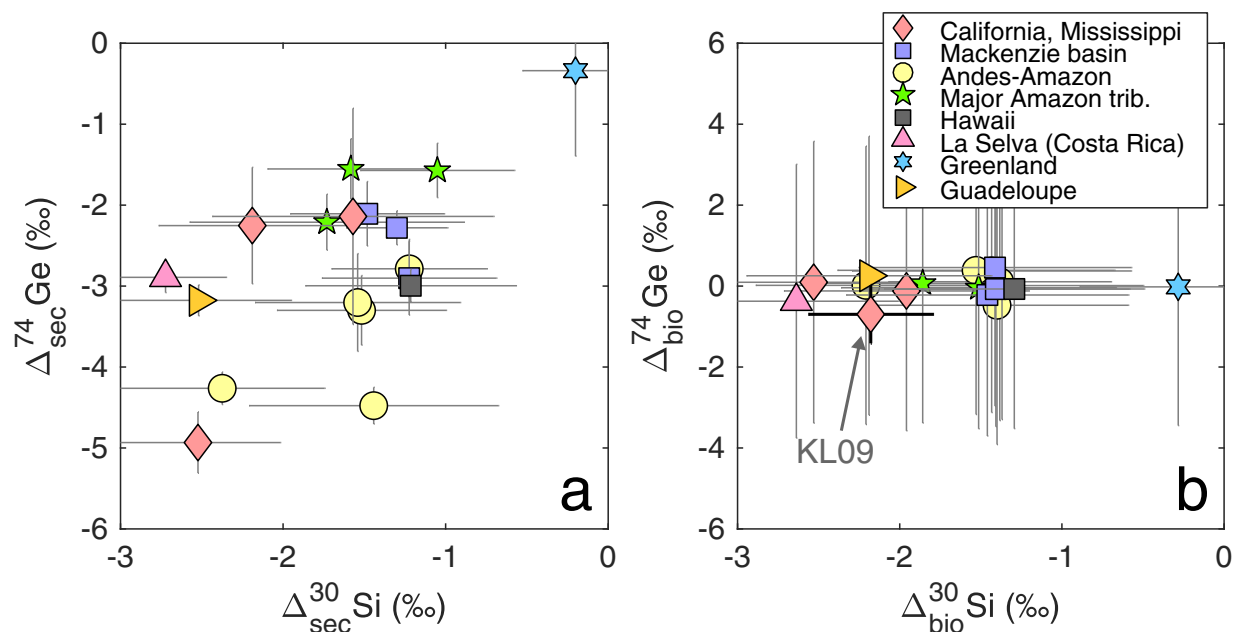


Figure 8: The relationship between the Si and Ge isotope fractionation factors associated with secondary weathering (a) and biological uptake (b). Symbols are plotted as medians and error bars as 1 standard deviation of the calculated range of values. Note that for most samples, the value of Δ_{bio} could not be accurately determined (i.e. the error bars span 1 st.dev. of the whole conservative range of pre-assigned values). The notable exception was the Lower Kern (KL09) sample, where biological fractionation was modeled as a Rayleigh process in a dam reservoir with additional constraints on $\delta^{74}\text{Ge}$ mass balance in the reservoir (Section 3.4.2).

can explain the majority of currently available riverine $\delta^{74}\text{Ge}_{\text{diss}}$ data. In the case of Si, most experimentally determined aluminosilicate and Fe- and Al-oxide $\Delta^{30}\text{Si}_{\text{sec}}$ factors fall in the -2 to 0 ‰ range (Frings et al., 2016), also in agreement with the majority of the values determined here (Fig. 8, Appendix Table C3).

3.4.3 Ge/Si-isotope fractionation model: limitations and implications

Fundamentally, river waters and sediments average processes taking place on a range of spatial and temporal scales within heterogeneous catchments. Inevitably, information is lost when large catchments are represented by a small number of samples, as was done in this study. This can hamper quantitative efforts, although in some cases, averaging by processes such as mixing of waters can be helpful in reducing complexity (see discussion above and Druhan & Maher (2017)).

Currently, most of the uncertainty in these modeling results is introduced by the poor constraints on $\alpha_{\text{sec}}^{\text{Ge/Si}}$ and especially $\alpha_{\text{bio}}^{\text{Ge/Si}}$ values, with the calculated f_{sec} and f_{bio} estimates particularly sensitive to these parameters. The range of $\alpha_{\text{bio}}^{\text{Ge/Si}}$ values reported for various plants is especially wide, spanning three orders of magnitude (Derry et al., 2005; Blecker et al., 2007; Meek et al., 2016, Table C2). Surveys of representative soils and plants are therefore required to obtain better catchment-specific estimates of $\alpha_{\text{bio}}^{\text{Ge/Si}}$.

In addition, analyses of primary and secondary mineral assemblages in river sediments (along

with relevant thermodynamic experimental data) could help significantly improve the catchment-averaged estimates of all α_{sec} parameters (assuming dominantly equilibrium fractionation). In the case of dominantly kinetic fractionation, the addition of time-series data and better constraints on water transit times within a catchment (again, along with relevant kinetic experimental data) would also result in more accurate estimates of fractionation factors.

Given all of the above, the results of this modeling effort should be treated as preliminary. However, this modeling framework serves as an example of how a fully integrated multi-proxy approach can be used to move away from purely qualitative observations, opening the possibility to quantitatively deconvolve multiple isotope-fractionating biogeochemical processes. Finally, obtaining robust locally or globally relevant constraints on biological uptake, silicate weathering, and their associated isotopic fractionation on the continents would greatly benefit paleorecord-based investigations of the climate-weathering feedback.

4 Conclusions

We have analyzed the dissolved $\delta^{74}\text{Ge}$ and Ge/Si composition of 31 rivers worldwide, including the Amazon, Changjiang, Mekong, and Mackenzie rivers. Combined with the previous dataset of Baronas et al. (2017a), the $\delta^{74}\text{Ge}$ values range from 0.9 to 5.5 ‰ with a discharge-weighted global average at 2.6 ± 0.5 ‰. Several samples of river suspended and bedload sediments exhibit $\delta^{74}\text{Ge}$ that is indistinguishable from silicate bedrock (0.4 - 0.8 ‰), consistent with low Ge solubility and transport predominantly in the solid phase. In contrast, we have observed fractionation in $\delta^{30}\text{Si}$ of bedload and suspended load samples due to sorting of particle sizes during transport in a large river system draining the eastern Andes.

A simple model coupling the fractionation of Ge/Si, $\delta^{74}\text{Ge}$, and $\delta^{30}\text{Si}$ has enabled us to attempt the first quantitative deconvolution of Ge and Si uptake by secondary mineral phases vs. biota (plants or freshwater diatoms). Modeling results indicate that, depending on the river, 12-54% (avg. 32%) of initially released Si is taken up biologically, whereas secondary phases remove 19-79 % (avg. 54 ‰), with 3-39% (avg. 13%) remaining in the dissolved phase. In contrast, most dissolved Ge is taken up by secondary phases (79-98 ‰). The isotopic fractionation factors associated with secondary phase uptake are estimated to range from -2.7 to -1.1 ‰ for $\delta^{30}\text{Si}$ and -4.9 to -1.6 ‰ for $\delta^{74}\text{Ge}$. The biological fractionation of Ge by freshwater diatoms was calculated as -0.7 ± 0.7 ‰.

Overall, we have demonstrated how a multi-proxy approach, in this case coupling Ge/Si, $\delta^{74}\text{Ge}$, and $\delta^{30}\text{Si}$ fractionation, can help put quantitative constraints on biogeochemical processes like the precipitation of secondary weathering phases and the biological uptake of solutes by living organisms.

5 Acknowledgements

Financial support was provided by US National Science Foundation (NSF) grants OCE 1061700 and OCE 1260692 to DEH. JJB was additionally supported by a CUAHSI Pathfinder graduate student fellowship, an InterRidge research fellowship, and a John Montagne Award from GSA Quaternary Geology and Geomorphology Division. The Andes-Amazon component of this work was supported by US NSF grants EAR 1455352 and EAR 1227192 to AJW. Support for OR was provided by the Institut Carnot Ifremer EDROME and LabexMer ANR-10-LABX-19-01. We thank Emmanuel Ponzevera for analytical assistance with Ge isotope measurements at Ifremer and Yi Hou for help with Si concentration analyses at USC. We are extremely grateful to the following people who helped collect the global river samples used in this study: Valier Galy, Sarah Rosengard, Paulina Piñedo-Gonzalez, Bernhard Peucker-Ehrenbrink, Mathieu Dellinger, Mia Bennett, Lincoln Pitcher, Gen Li, Shilei Li, Sophie Opfergelt, Kevin Burton, Philip Pogge von Strandmann, Rachael James, and Jane Hammond. Sample collection in Peru was accomplished with additional help from Kathryn Clark, Sarah Feakins, Emily Burt, Camilo Ponton, and a number of field assistants over the years, as well as field support from ACCA Peru, Manu Learning Centre, and Incaterra. We also thank Patrick Frings for sharing his riverine $\delta^{30}\text{Si}$ data compilation. This manuscript was improved by the constructive comments of Philip Pogge von Strandmann and two anonymous reviewers. We thank Derek Vance for editorial handling.

References

- Allard T, Menguy N, Salomon J, Calligaro T, Weber T, Calas G, Benedetti MF (2004) Revealing forms of iron in river-borne material from major tropical rivers of the Amazon Basin (Brazil). *Geochimica et Cosmochimica Acta* 68:3079–3094.
- Baronas JJ, Hammond DE, Berelson WM, McManus J, Severmann S (2016) Germanium-silicon fractionation in a river-influenced continental margin: The Northern Gulf of Mexico. *Geochimica et Cosmochimica Acta* 178:124–142.
- Baronas JJ, Hammond DE, McManus J, Wheat CG, Siebert C (2017a) A global Ge isotope budget. *Geochimica et Cosmochimica Acta* 203:265–283.
- Baronas JJ, Torres MA, Clark KE, West AJ (2017b) Mixing as a driver of temporal variations in river hydrochemistry: 2. Major and trace element concentration dynamics in the Andes-Amazon transition. *Water Resources Research* 53.
- Baronas JJ (2017) Germanium and silicon isotope geochemistry in terrestrial and marine low-temperature environments Ph.D. diss., University of Southern California.
- Bayon G, Delvigne C, Ponzevera E, Borges A, Darchambeau F, De Deckker P, Lambert T, Monin L, Toucanne S, André L (2018) The silicon isotopic composition of fine-grained river sediments and its relation to climate and lithology. *Geochimica et Cosmochimica Acta* 229:147–161.
- Berner R, Lasaga A, Garrels R (1983) The carbonate-silicate geochemical cycle and its effect on atmospheric carbon dioxide over the past 100 million years. *American Journal of Science* 283:641–683.
- Bernstein LR, Waychunas GA (1987) Germanium crystal chemistry in hematite and goethite from the Apex Mine, Utah, and some new data on germanium in aqueous solution and in stottite. *Geochimica et Cosmochimica Acta* 51:623–630.
- Blecker SW, King SL, Derry LA, Chadwick OA, Ippolito JA, Kelly EF (2007) The ratio of germanium to silicon in plant phytoliths: Quantification of biological discrimination under controlled experimental conditions. *Biogeochemistry* 86:189–199.
- Bouchez J, von Blanckenburg F, Schuessler JA (2013) Modeling novel stable isotope ratios in the weathering zone. *American Journal of Science* 313:267–308.
- Bouchez J, Gaillardet J, France-Lanord C, Maurice L, Dutra-Maia P (2011) Grain size control of river suspended sediment geochemistry: Clues from Amazon River depth profiles. *Geochemistry, Geophysics, Geosystems* 12:n/a–n/a.
- Burton J, Culkin F, Riley J (1959) The abundances of gallium and germanium in terrestrial materials. *Geochimica et Cosmochimica Acta* 16:151–180.
- Cornelis JT, Delvaux B, Georg RB, Lucas Y, Ranger J, Opfergelt S (2011) Tracing the origin of dissolved silicon transferred from various soil-plant systems towards rivers: a review. *Biogeosciences* 8:89–112.

- Dellinger M, Bouchez J, Gaillardet J, Faure L, Moureau J (2017) Tracing weathering regimes using the lithium isotope composition of detrital sediments. *Geology* 45:411–414.
- Dellinger M, Gaillardet J, Bouchez J, Calmels D, Louvat P, Dosseto A, Gorge C, Alanoca L, Maurice L (2015) Riverine Li isotope fractionation in the Amazon River basin controlled by the weathering regimes. *Geochimica et Cosmochimica Acta* 164:71–93.
- Dellinger M, Gaillardet J, Bouchez J, Calmels D, Galy V, Hilton RG, Louvat P, France-Lanord C (2014) Lithium isotopes in large rivers reveal the cannibalistic nature of modern continental weathering and erosion. *Earth and Planetary Science Letters* 401:359–372.
- Derry LA, Kurtz AC, Ziegler K, Chadwick OA (2005) Biological control of terrestrial silica cycling and export fluxes to watersheds. *Nature* 433:728–31.
- Derry LA, Pett-Ridge JC, Kurtz AC, Troester JW (2006) Ge/Si and $^{87}\text{Sr}/^{86}\text{Sr}$ tracers of weathering reactions and hydrologic pathways in a tropical granitoid system. *Journal of Geochemical Exploration* 88:271–274.
- Ding T, Wan D, Wang C, Zhang F (2004) Silicon isotope compositions of dissolved silicon and suspended matter in the Yangtze River, China. *Geochimica et Cosmochimica Acta* 68:205–216.
- Druhan JL, Maher K (2017) The influence of mixing on stable isotope ratios in porous media: A revised Rayleigh model. *Water Resources Research* 53:1–24.
- Edmond J, Palmer M, Measures C, Grant B, Stallard R (1995) The fluvial geochemistry and denudation rate of the Guayana Shield in Venezuela, Colombia, and Brazil. *Geochimica et Cosmochimica Acta* 59:3301–3325.
- Escoube R, Rouxel OJ, Luais B, Ponzevera E, Donard OF (2012) An Intercomparison Study of the Germanium Isotope Composition of Geological Reference Materials. *Geostandards and Geoanalytical Research* 36:149–159.
- Frings PJ, Clymans W, Fontorbe G, De La Rocha CL, Conley DJ (2016) The continental Si cycle and its impact on the ocean Si isotope budget. *Chemical Geology* 425:12–36.
- Froelich P, Blanc V, Mortlock R, Chillrud S, Dunstan W, Udomkit A, Peng T (1992) River fluxes of dissolved silica to the ocean were higher during glacials: Ge/Si in diatoms, rivers, and oceans. *Paleoceanography* 7:739–767.
- Gaillardet J, Dupré B, Louvat P, Allègre C (1999) Global silicate weathering and CO₂ consumption rates deduced from the chemistry of large rivers. *Chemical Geology* 159:3–30.
- Gaillardet J, Viers J, Dupré B (2014) Trace Elements in River Waters In *Treatise on Geochemistry*, chapter 7.7, pp. 195–235. Elsevier, 2 edition.
- Georg R, Reynolds B, Frank M, Halliday A (2006a) Mechanisms controlling the silicon isotopic compositions of river waters. *Earth and Planetary Science Letters* 249:290–306.
- Georg R, Reynolds B, Frank M, Halliday A (2006b) New sample preparation techniques for the determination of Si isotopic compositions using MC-ICPMS. *Chemical Geology* 235:95–104.

- Georg R, Reynolds B, West A, Burton K, Halliday A (2007) Silicon isotope variations accompanying basalt weathering in Iceland. *Earth and Planetary Science Letters* 261:476–490.
- Gislason SR, Arnorsson S, Armannsson H (1996) Chemical weathering of basalt in Southwest Iceland; effects of runoff, age of rocks and vegetative/glacial cover. *American Journal of Science* 296:837–907.
- Guillermic M, Lalonde SV, Hendry KR, Rouxel OJ (2017) The isotope composition of inorganic germanium in seawater and deep sea sponges. *Geochimica et Cosmochimica Acta* 212:99–118.
- Han Y, Huh Y, Derry L (2015) Ge/Si ratios indicating hydrothermal and sulfide weathering input to rivers of the Eastern Tibetan Plateau and Mt. Baekdu. *Chemical Geology* 410:40–52.
- Hofmann AW (1988) Chemical differentiation of the Earth: the relationship between mantle, continental crust, and oceanic crust. *Earth and Planetary Science Letters* 90:297–314.
- Hughes H, Sondag F, Santos R, André L, Cardinal D (2013) The riverine silicon isotope composition of the Amazon Basin. *Geochimica et Cosmochimica Acta* 121:637–651.
- Kurtz A, Derry L, Chadwick O (2002) Germanium-silicon fractionation in the weathering environment. *Geochimica et Cosmochimica Acta* 66:1525–1537.
- Li XF, Liu Y (2010) First-principles study of Ge isotope fractionation during adsorption onto Fe(III)-oxyhydroxide surfaces. *Chemical Geology* 278:15–22.
- Meek K, Derry L, Sparks J, Cathles L (2016) $^{87}\text{Sr}/^{86}\text{Sr}$, Ca/Sr, and Ge/Si ratios as tracers of solute sources and biogeochemical cycling at a temperate forested shale catchment, central Pennsylvania, USA. *Chemical Geology* .
- Milliman JD, Farnsworth KL (2011) Runoff, erosion, and delivery to the coastal ocean In *River Discharge to the Coastal Ocean*, pp. 13–69. Cambridge University Press, Cambridge.
- Mortlock R, Froelich P (1987) Continental weathering of germanium: Ge/Si in the global river discharge. *Geochimica et Cosmochimica Acta* 51:2075–2082.
- Murnane R, Stallard R (1990) Germanium and silicon in rivers of the Orinoco drainage basin. *Nature* 344:749–752.
- Pokrovski GS, Schott J (1998) Experimental study of the complexation of silicon and germanium with aqueous organic species: implications for germanium and silicon transport and Ge/Si ratio in natural waters. *Geochimica et Cosmochimica Acta* 62:3413–3428.
- Pokrovsky OS, Galy A, Schott J, Pokrovski GS, Mantoura S (2014) Germanium isotope fractionation during Ge adsorption on goethite and its coprecipitation with Fe oxy(hydr)oxides. *Geochimica et Cosmochimica Acta* 131:138–149.
- Pokrovsky O, Pokrovski G, Schott J, Galy A (2006) Experimental study of germanium adsorption on goethite and germanium coprecipitation with iron hydroxide: X-ray absorption fine structure and macroscopic characterization. *Geochimica et Cosmochimica Acta* 70:3325–3341.

- Rayleigh L (1902) LIX. On the distillation of binary mixtures. *The London, Edinburgh, and Dublin Philosophical Magazine and Journal of Science* 4:521–537.
- Raymo ME, Ruddiman WF (1992) Tectonic forcing of late Cenozoic climate. *Nature* 359:117–122.
- Rouxel O, Galy A, Elderfield H (2006) Germanium isotopic variations in igneous rocks and marine sediments. *Geochimica et Cosmochimica Acta* 70:3387–3400.
- Rouxel OJ, Luais B (2017) Germanium Isotope Geochemistry. *Reviews in Mineralogy and Geochemistry* 82:601–656.
- Rudnick R, Gao S (2014) Composition of the Continental Crust In *Treatise on Geochemistry*, Vol. 4, pp. 1–51. Elsevier, 2 edition.
- Savage PS, Georg RB, Williams HM, Halliday AN (2013) The silicon isotope composition of the upper continental crust. *Geochimica et Cosmochimica Acta* 109:384–399.
- Scribner AM, Kurtz AC, Chadwick OA (2006) Germanium sequestration by soil: Targeting the roles of secondary clays and Fe-oxyhydroxides. *Earth and Planetary Science Letters* 243:760–770.
- Siebert C, Hammond DE, Ross A, McManus J (2011) Erratum to C. Siebert, A. Ross and J. McManus (2006) "Germanium isotope measurements of high-temperature geothermal fluids using double-spike hydride generation MC-ICP-MS", *Geochimica et Cosmochimica Acta* 70, 3986-3995. *Geochimica et Cosmochimica Acta* 75:6267–6269.
- Siebert C, Nögler T, Kramers J (2001) Determination of molybdenum isotope fractionation by double-spike multicollector inductively coupled plasma mass spectrometry. *Geochemistry Geophysics Geosystems* 2.
- Siebert C, Ross A, McManus J (2006) Germanium isotope measurements of high-temperature geothermal fluids using double-spike hydride generation MC-ICP-MS. *Geochimica et Cosmochimica Acta* 70:3986–3995.
- Stevenson EI, Fantle MS, Das SB, Williams HM, Aciego SM (2017) The iron isotopic composition of subglacial streams draining the Greenland ice sheet. *Geochimica et Cosmochimica Acta* 213:237–254.
- Tipper ET, Calmels D, Gaillardet J, Louvat P, Capmas F, Dubacq B (2012) Positive correlation between Li and Mg isotope ratios in the river waters of the Mackenzie Basin challenges the interpretation of apparent isotopic fractionation during weathering. *Earth and Planetary Science Letters* 333-334:35–45.
- Torres MA, Baronas JJ, Clark KE, Feakins SJ, West AJ (2017) Mixing as a driver of temporal variations in river hydrochemistry: 1. Insights from conservative tracers in the Andes-Amazon transition. *Water Resources Research* 53:1–18.
- Torres MA, West AJ, Clark KE (2015) Geomorphic regime modulates hydrologic control of chemical weathering in the Andes-Amazon. *Geochimica et Cosmochimica Acta* 166:105–128.

Torres MA, West AJ, Clark KE, Paris G, Bouchez J, Ponton C, Feakins SJ, Galy V, Adkins JF (2016) The acid and alkalinity budgets of weathering in the Andes–Amazon system: Insights into the erosional control of global biogeochemical cycles. *Earth and Planetary Science Letters* 450:381–391.

von Blanckenburg F, Schuessler Ja (2014) Element Cycling in the Critical Zone as Viewed by New Isotope Tools. *Procedia Earth and Planetary Science* 10:173–178.

Wimpenny J, Burton KW, James RH, Gannoun A, Mokadem F, Gíslason SR (2011) The behaviour of magnesium and its isotopes during glacial weathering in an ancient shield terrain in West Greenland. *Earth and Planetary Science Letters* 304:260–269.

Wimpenny J, Colla CA, Yu P, Yin QZ, Rustad JR, Casey WH (2015) Lithium isotope fractionation during uptake by gibbsite. *Geochimica et Cosmochimica Acta* 168:133–150.

Wimpenny J, James RH, Burton KW, Gannoun A, Mokadem F, Gíslason SR (2010) Glacial effects on weathering processes: New insights from the elemental and lithium isotopic composition of West Greenland rivers. *Earth and Planetary Science Letters* 290:427–437.

A Appendix: Detailed methods

A1 Element concentration analyses

Major cation (Na, K, Ca, Mg) and Si concentrations in river water were measured using an Agilent 4100 Microwave Plasma-Optical Emission Spectrometer (MP-OES) at the University of Southern California. Additional Si analyses were performed using molybdate blue colorimetry (Mullin & Riley, 1955). The values obtained via both methods agreed within uncertainty. Precision and accuracy were assessed by analyzing ION-915 (Environment Canada) certified reference material interspersed with samples. Reproducibility of replicate analyses was better than 10% (2σ) for all analytes.

The methods described below apply to all samples except the Madeira River data (Table B1, Fig. 3), for which the methods are described in Bouchez et al. (2011). Briefly, the Madeira River sediments were aliquoted after recovery (filtration at 0.22 μm , drying), ground, digested by lithium borate fusion, and analyzed by ICP-MS for trace elements (Ge data) and ICP-OES for major elements (Si data) at the Service d'Analyse des Roches et Minéraux (SARM), Vandoeuvre-les-Nancy, France.

Si concentrations in solid samples were determined in one of two ways: 1) quadrupole ICP-MS at Ifremer on aliquots from HNO_3 +HF digestions described below; or 2) after NaOH fusion and dissolution in Teflon-distilled HNO_3 using the method described below, followed by molybdate blue colorimetry. A number of samples were analyzed using both methods, and some of the Andes-Amazon rock and bedload samples have also been previously analyzed using XRF (Torres et al., 2016). The Si concentrations agree within 10% using all three methods.

Ge concentrations in river water were measured using isotope dilution hydride generation inductively coupled plasma mass spectrometry (ID-HG-IPC-MS) on a Thermo Element 2, as described in Mortlock & Froelich (1996) and modified by Hammond et al. (2000) and Baronas et

al. (2016), with a typical 2 S.D. uncertainty of <5%. Accuracy and precision were assessed by measurements of NIST 3120a and internal river water standards analyzed alongside the samples at similar concentrations. The procedural blank was variable but typically around 1-2 pg (15-30 fmol) Ge. Ge concentrations in solid samples were determined during Ge isotope analyses, as described below.

A2 Si isotope analyses

Fusion. Si isotope composition in solid samples was analyzed using a method adapted from Georg et al. (2006b). Briefly, 10-20 mg of sample was fused with ~200 mg trace-grade NaOH in silver crucibles at 710 °C. The crucibles with fusion cakes were sonicated for 30 min in 20 mL doubly-deionized water (DDIW) and left to dissolve for 24h. The solution was then transferred into 500 mL polyethylene bottles, carefully rinsing to ensure complete recovery, diluted to 400-500 mL with DDIW, and acidified with 5 mL trace grade conc. HNO₃. This method is noted as "NaOH fus." in Table 2. A number of organic-rich shale samples were ashed in graphite crucibles at 550 °C for 2h prior to NaOH fusion ("ash. + NaOH fus." in Table 2). In both cases, the fused samples were then processed in the same way as river water samples. The Si concentrations and $\delta^{30}\text{Si}$ values determined using both fusion methods were identical within uncertainty.

Cation-exchange chromatographic separation. A procedure adapted from Georg et al. (2006b) was used for dissolved samples and for the solutions obtained from fusion. All reagents used were either in-house Teflon-distilled or Optima-grade. A 10 mL column was filled with 1.8 mL (wet volume in 0.5M HNO₃) BioRad AG50W-X12 (200-400 mesh) resin. The column was washed with 15 mL DDIW, 3.6 mL 0.15M HF (new resin only), 10 mL 3M HCl, 5 mL 6M HCl, 4 mL 11M HCl, 5 mL 6M HCl, 5 mL 3M HCl, and 2x10 mL DDIW. Between 0.3 and 8 mL sample was then loaded onto the column and eluted with 4-10 mL DDIW to obtain a final solution of 1.5 ppm Si. Larger batches of several standards were prepared by eluting with up to 40 mL DDIW to obtain 3 ppm Si solutions that were then further diluted to 1.5 ppm. All bracketing standard and reference material aliquots were purified using the same cation-exchange method as the samples. The columns were reused up to a maximum of four times, at which point the resin was replaced.

MC-ICP-MS. Si isotope measurements were performed on a Thermo Neptune instrument at the Water Quality Centre at Trent University. An Elemental Scientific ApexQ was used for sample introduction at a rate of 300 $\mu\text{L}/\text{min}$. The Neptune was operated at medium resolution. ^{28}Si , ^{29}Si , and ^{30}Si were measured in cups C, H2, and H3, respectively. The measurements were done at the flat part of the low mass peak shoulder that is free of the major interference from $^{14}\text{N}^{16}\text{O}^+$. The measurement window was manually re-positioned at least once within each analytical session but the drift was never more than ± 0.0002 mass units. Sample runs were bracketed with concentration-matched NBS-28 standard solution prepared using the same fusion and cation exchange methods described above. Each sample was measured as 2-4 bracketed replicate runs consisting of 30 cycles of 8s each. This resulted in 8-16 min of counting statistics for each sample at typical signal intensities of 8-18 V ^{28}Si . The $\delta^{30}\text{Si}$ values are reported as the sample $^{30}\text{Si}/^{28}\text{Si}$ ratio normalized to the bracketing NBS-28 standard. Mass dependence was ensured by comparing the $\delta^{30}\text{Si}$ and $\delta^{29}\text{Si}$ values of each run, which were within 0.2 ‰ (in terms of $\delta^{30}\text{Si}$) of the mass-dependent fractionation line for the vast majority of the measurements (Table A1). Blanks were typically less than 80 mV or 1% of sample signal intensity. Several of different reference materials were analyzed

multiple times interspersed with the samples, all of which agreed well with previously reported values (Table A3). The measurement uncertainty is reported as the internal 2σ standard error of sample replicates, or 2σ standard deviation of all NBS-28 bracketing standard measurements within a given analytical session, whichever is higher.

A3 Ge isotope analyses

River water. 0.2 to 4.7 L of filtered river water containing 2-100 ng of Ge was acidified with trace clean HNO_3 , and spiked with a Ge isotope double spike ($^{73}\text{Ge}/^{70}\text{Ge} \approx 1$, previously calibrated and used by Escoube et al. (2012, 2015)) in a spike/sample Ge mass ratio of 1-2 and a purified FeCl_3 solution to obtain a Fe concentration of ~ 0.2 mmol/L. The samples were well mixed, and allowed to equilibrate for at least 16h. Next, $\text{Fe}(\text{OH})_3$ floc was precipitated either by adding Optima-grade NH_4OH solution or bubbling pure NH_3 gas through the sample until the solution reached a pH of 8-10. The floc was collected by settling and centrifugation, redissolved in 2 mL concentrated Teflon-distilled HNO_3 and diluted to 10 mL with DDIW. The samples were then dried down, redissolved in 1 mL concentrated Optima-grade HF and diluted to 30 mL with DDIW to obtain a final 1M HF solution. They were then purified through anion exchange columns as described below. The procedural blank was determined by processing spiked DDIW and ranged from 0.01 to 0.3 ng Ge.

Rocks and sediments. A method adapted from Rouxel et al. (2006) was used for solid sample digestion. 10-130 mg of dried ground sample containing 30-300 ng of Ge was weighed into Teflon digestion vessels and spiked with a Ge isotope double spike ($^{73}\text{Ge}/^{70}\text{Ge} \approx 1$) in a spike/sample Ge mass ratio of 1-2. Two slightly different digestion methods were tested to ensure that organic-rich shale samples were fully dissolved. Regular digestion ("HF"; Tables A3 and 2) was done by adding 5 mL of concentrated Teflon-distilled HNO_3 and heating to 90 °C for 16h. The samples were then dried down and 2-3 mL of MQ (to ensure all of sample was fully wetted) and 1m L concentrated trace metal-grade HF were added. The vessels were tightly capped and left on a 70 °C hotplate for 20-24h. After cooling, the samples were diluted to 30 mL with DDIW to obtain a final 1M HF solution that was purified through column anion exchange columns as described below. A second batch of samples including replicates (" HNO_3 +HF"; Tables A3 and 2) was digested by adding 10 mL concentrated Teflon-distilled HNO_3 and heating in a pressurized Teflon vessel at 90 °C for 48h. Then, 1mL of Optima-grade H_2O_2 was added and heated uncapped at 70 °C until dry. After cooling, 4 mL DDIW and 1mL concentrated trace-metal grade HF were added and samples were digested at 70 °C for 48 h. After cooling, the samples were diluted to 30 mL with DDIW to obtain a final 1M HF solution that was purified through column anion exchange columns as described below. The full procedural blank was determined by processing only Ge double spike and was below detection for the "HF" batch and 1.7 ng Ge for the " HNO_3 +HF" batch. The $\delta^{74}\text{Ge}$ values determined using both digestion methods were identical within uncertainty, indicating that ashing is not necessary to extract all Ge contained in shales.

Anion-exchange chromatographic separation. A procedure adapted from Rouxel et al. (2006) was used. All reagents used were either in-house Teflon-distilled or Optima-grade. A 10 mL column was loaded with 1.8 mL (wet volume) of BioRad AG1-X8 resin, washed with 10 mL of 3M HNO_3 , 0.28M HNO_3 , and DDIW in sequence, and conditioned with 5 mL 1M HF. Samples in 1M HF solution as prepared above were centrifuged to separate insoluble fluorides. The presence

Table A1: Comparison of measured $\delta^{30}\text{Si}$ and $\delta^{29}\text{Si}$ values. A regression of all sample analyses yields a slope of $\delta^{29}\text{Si} = 0.5125 \times \delta^{30}\text{Si}$.

Sample ID	$\delta^{29}\text{Si}$, ‰	$\delta^{30}\text{Si}$, ‰
GRO001622	0.84 ± 0.08	1.70 ± 0.15
KL09	2.11 ± 0.08	4.23 ± 0.20
SGN13	1.1 ± 0.08	2.13 ± 0.15
CAN10-(11+14)	0.55 ± 0.08	1.15 ± 0.15
CAN10-(46+48)	0.46 ± 0.08	0.96 ± 0.22
CAN10-(03+05)	0.45 ± 0.1	0.96 ± 0.15
FR15	0.53 ± 0.12	1.12 ± 0.15
JO-14	-0.07 ± 0.08	-0.12 ± 0.15
OA14-2	0.45 ± 0.12	0.86 ± 0.15
YR15	0.55 ± 0.08	1.13 ± 0.15
AN-14-(42-44)	0.62 ± 0.08	1.22 ± 0.15
MMD-02	0.52 ± 0.08	0.94 ± 0.15
MMD-28	0.4 ± 0.08	0.82 ± 0.15
MMD-32	0.55 ± 0.1	1.08 ± 0.15
MMD-29	0.38 ± 0.08	0.74 ± 0.15
MMD-34	0.8 ± 0.08	1.53 ± 0.15
AM14-36	0.51 ± 0.08	1.02 ± 0.15
AM14-40	0.26 ± 0.08	0.56 ± 0.15
AM06-(23-30)	0.42 ± 0.08	0.88 ± 0.15
WP-13	-0.13 ± 0.08	-0.25 ± 0.15
ROCK-1	-0.35 ± 0.08	-0.62 ± 0.15
ROCK-2	-0.31 ± 0.11	-0.60 ± 0.15
ROCK-4	-0.37 ± 0.08	-0.67 ± 0.15
R2250_21_03	-0.28 ± 0.14	-0.55 ± 0.15
S200511	-0.27 ± 0.08	-0.53 ± 0.17
RKOS-0550	-0.23 ± 0.08	-0.48 ± 0.15
CMD-29_3m	-0.2 ± 0.1	-0.37 ± 0.15
CMD-29_6m	-0.17 ± 0.08	-0.35 ± 0.15
CMD-29_8m	-0.15 ± 0.08	-0.30 ± 0.15
CMD-29_10m	-0.11 ± 0.08	-0.21 ± 0.15
RPtMA-0177	-0.12 ± 0.12	-0.24 ± 0.15
BHVO-1	-0.25 ± 0.15	-0.37 ± 0.26
BHVO-2	-0.17 ± 0.07	-0.32 ± 0.09
SCo-1	-0.2 ± 0.18	-0.26 ± 0.01
Diatomite	0.62 ± 0.09	1.22 ± 0.14
IRMM-018	-0.82 ± 0.05	-1.57 ± 0.08

or amount of insoluble fluorides at this stage did not appear to affect the final Ge recovery. After centrifugation, 10-29 mL of solution was carefully added to columns. The remaining matrix was eluted with 5 mL of 1M HF followed by 3 mL of DDIW, leaving fluorinated Ge retained on the column. Ge was then eluted with 10 mL 0.28M HNO₃. If required, the solution was dried down and redissolved in a smaller volume of 0.28M HNO₃ to obtain the 2-10 ppb Ge concentration required for isotope measurements. Each column was reused 4-5 times, except when retention of DOC from the previous sample was observed based on the color, in which case the resin was replaced. Ge blanks from reused resin were below detection limit. Ge recovery ranged from 20 to 100%, and was in the 70-90% range for most river samples and in the 100±7% range for solid samples. Incomplete recovery of river samples was most likely due to variable Ge co-precipitation efficiency with Fe(OH)₃, due to variable precipitation rates, final pH and natural sample matrices, as well as some loss during co-precipitate recovery from the solution. Importantly, incomplete recovery does not affect the measured $\delta^{74}\text{Ge}$ values, as all samples were double-spiked prior to sample preparation. Previous tests have shown that this method separates the methylated and the inorganic Ge species, retaining only the latter for isotopic analyses (Guillermic et al., 2017).

HG-MC-ICP-MS. Ge isotope analyses were performed on a Thermo Neptune multi-collector ICP-MS at Ifremer using a method adapted from Rouxel et al. (2006) and Escoube et al. (2015). Sample solutions of 2-10 ppb natural Ge in 0.28M HNO₃ were introduced into an online hydride generation system (CETAC HGX-200) at a rate of 150 $\mu\text{L}/\text{min}$ where they were mixed with 0.25 M NaBH₄ solution (in 1.5 M NaOH) introduced at an equal rate. The dissolved Ge(OH)₄ species was reduced to gaseous GeH₄ and transported into the ICP-MS torch using Ar carrier gas. The Neptune MC-ICP-MS was operated in low mass resolution mode, measuring ⁷⁰Ge, ⁷²Ge, ⁷³Ge, and ⁷⁴Ge in L2, C, H1 and H2 cups, respectively. In addition, L4, L3, L1 and H4 cups were also monitored for ⁶⁸Zn (possible interference as ⁷⁰Zn), ⁶⁹Ga, ⁷¹Ga (possible interferences at m/z 70), and ⁷⁷Se (possible interference as ⁷⁴Se), respectively. No interferences were detected in any of the runs. The samples were bracketed using a NIST-3120a standard solution that had a total Ge concentration generally within ~20 % of the bracketed sample, and was double-spiked to have a spike/sample ratio within ~20 % of the bracketed sample. Each sample or standard run consisted of 6 measurement blocks each lasting 2 min (30 cycles of 4 s each), and in most cases 4-5 blocks displaying the most stable signal were retained. Therefore, each measurement represents 8-10 min of counting statistics at signal intensities ranging from 0.4 to 6 V at ⁷⁴Ge (depending on Ge concentration in sample solution, instrument tuning, and the age of NaBH₄ solution). The $\delta^{74}\text{Ge}$ values are calculated for each block using the double-spike data reduction routine of Siebert et al. (2001) and are reported in ‰ as ⁷⁴Ge/⁷⁰Ge sample ratio normalized to the average ⁷⁴Ge/⁷⁰Ge ratio of bracketing NIST 3120a measurements. This method also yields Ge concentration values based on the measured spike/sample ratio. The measurement uncertainty is reported as the internal 2 σ standard error of the used sample blocks, or 2 σ standard deviation of all NIST 3120a bracketing standard measurements within a given analytical session, whichever is higher.

A4 Cross-laboratory calibration of Ge and Si isotope analyses

The accuracy of Ge and Si concentration and isotope analyses was confirmed by re-analyzing several reference materials and samples that have been previously analyzed in other studies. Regardless of the digestion method (see above for details), the Ge and Si concentrations, $\delta^{74}\text{Ge}$,

Table A2: Comparison of analytical $\delta^{74}\text{Ge}$ methods.

Study	this study	Baronas et al. (2017a)
Double-spike	Ifremer aliquot; $^{73}\text{Ge}/^{70}\text{Ge} \approx 1$; calibrated and used by Escoube et al. (2012, 2015)	OSU aliquot; $^{73}\text{Ge}/^{70}\text{Ge} \approx 1$; calibrated and used by Siebert et al. (2006, 2011)
Ge co-precipitation method	$\text{Fe}(\text{OH})_3$	$\text{Mg}(\text{OH})_2$
Purification	AG1-X8 anion exchange column (Rouxel et al., 2006)	Offline hydride generation and GeH_4 capture in Tedlar gas bags
Sample introduction	Online hydride generation (constant rate) coupled to MC-ICP-MS	Pressure-controlled GeH_4 injection at variable rate
MC-ICP-MS	Thermo Neptune (Ifremer, France)	Nu Instruments Plasma (Oregon State University, USA)
Range of ^{74}Ge signal intensities (among all samples)	0.4 - 6.0 V	0.02 - 1.5 V

and $\delta^{30}\text{Si}$ compositions of solids reported in this study agree within uncertainty with previously published values (Table A3).

Eight of the dissolved river samples previously analyzed for $\delta^{74}\text{Ge}$ by Baronas et al. (2017a) have also been re-analyzed using the method described above. The method used by Baronas et al. (2017a) relied on offline hydride generation, where methylated and inorganic Ge hydride species were separated chromatographically using a liquid N_2 trap and the inorganic species were collected in Tedlar bags for later analysis on a Nu Plasma MC-ICP-MS at Oregon State University. The differences in the methodology are summarized in Table A2. All sample replicates agree within ~ 0.5 ‰ and fall within the reported external 2 S.D. reproducibility, with the exception of the Lower Kern river for which the two reported values are very slightly outside of their 2 S.D. ranges (Table 1). Overall, this good agreement is notable, considering that the two methods employed in these studies use very different approaches to purify and analyze the samples. The high degree of consistency between these techniques most likely stems from the use of a double isotope spike that corrects for any mass-dependent fractionation that occurs during sample preparation and measurement.

Table A3: Ge and Si concentration and isotope analyses compared to reference values.

Reference material	ID	Digestion method	Ge, µg/g		Si, g/g		Ge/Si, µmol/mol	δ ⁷⁴ Ge, ‰		δ ³⁰ Si, ‰	
			<i>this study</i>	<i>prev.</i> ^a	<i>this study</i>	<i>cert.</i> ^b		<i>this study</i>	<i>prev.</i> ^a	<i>this study</i>	<i>prev.</i> ^c
USGS Dunite	DTS-1	HF	0.79	0.75 - 0.88	0.197	0.189	1.55	0.63 ± 0.23	0.64 ± 0.26	--	--
USGS Dunite	DTS-1	HNO ₃ +HF	0.81		0.191		1.65	0.58 ± 0.06		--	--
USGS Icelandic Basalt	BIR-1	HF	1.55	1.40 - 1.53	0.235	0.224	2.55	0.70 ± 0.08	0.62 ± 0.13	--	--
USGS Icelandic Basalt	BIR-1	HNO ₃ +HF	1.55		0.216		2.78	0.53 ± 0.08		--	--
USGS Hawaiian Basalt	BHVO-1	NaOH fus. (B3)	--	1.55, 1.64	0.253	0.233	(2.44)	--	0.55 ± 0.15	-0.37 ± 0.26	-0.29 ± 0.16
USGS Hawaiian Basalt	BHVO-2	NaOH fus. (Trent)	--	1.53	--	0.233	(2.54)	--	0.51 ± 0.10	-0.32 ± 0.09	-0.29 ± 0.11
USGS Devonian Ohio Shale	SDO-1	HNO ₃ +HF	0.81	--	0.203	0.230	1.55	0.79 ± 0.08	--	--	--
USGS Devonian Ohio Shale	SDO-1 ashed	HNO ₃ +HF	2.03 ^d	--	0.256		3.06	0.81 ± 0.08	--	--	--
USGS Cody Shale	SCO-1	NaOH fus. (B3)	--	--	0.253	0.294	--	--	--	-0.26 ± 0.15	--
Quartz	IRMM-018	--	--	--	--	--	--	--	--	-1.57 ± 0.08	-1.63 ± 0.15
Diatomite standard	Diatomite	--	--	--	--	--	--	--	--	1.22 ± 0.14	1.23 ± 0.16

^a Escoube et al. (2012)

^b Certified USGS value (crustal.usgs.gov)

^c Georg et al. (2009)

^d Uncorrected for mass loss during ashing.

B1 Appendix: Supplementary data

Table B1: Suspended and bedload sediment composition of the Madeira River at its confluence with the Amazon mainstem (Foz Madeira).

Sample ID	Date	Lat., °	Long., °	Type	Depth, m	SPM, mg/L	Ge, µg/g	Si, g/g	Ge/Si, µmol/mol
AM05_15	2005-06-06	03°27'00,9"	58°48'30,1"	Susp. load	23	94	2.05	0.27	2.93
AM05_16	2005-06-07	03°27'00,9"	58°48'30,1"	Susp. load	18	85	1.96	0.26	2.86
AM05_17	2005-06-06	03°27'57,6"	58°48'34,7"	Susp. load	12	74	2.13	0.26	3.13
AM05_18	2005-06-06	03°27'56,8"	58°48'33,6"	Susp. load	8	61	2.33	0.25	3.57
AM05_19	2005-06-06	03°27'56,8"	58°48'33,6"	Susp. load	3	49	2.20	0.25	3.47
AM05_20	2005-06-06	--	--	Bedload	28	--	1.47	0.40	1.43
AM05_21	2005-06-06	03°27'22,5"	58°47'57,9"	Susp. load	21	101	2.29	0.26	3.40
AM05_22	2005-06-06	03°27'19,8"	58°47'59,0"	Susp. load	15	88	2.13	0.26	3.11
AM05_23	2005-06-06	03°27'23,7"	58°47'56,6"	Susp. load	3	71	2.26	0.25	3.44
AM05_24	2005-06-06	--	--	Bedload (fine)	21	--	1.96	0.32	2.36

Table B2: Major dissolved ion concentrations in the studied rivers.

River	Sample ID	Na, μmol/L	K, μmol/L	Ca, μmol/L	Mg, μmol/L	Cl μmol/L	SO ₄ , μmol/L	Reference
<u>North America</u>								
Mississippi* (Aug 2011)	MI11	1369	137	1382	884	--	--	Baronas et al. (2017a)
Mississippi* (Jul 2015)	GRO001622	835	101	988	434	705	394	Peucker-Ehrenbrink et al., unpub.
Kaweah	KW13	292	39	--	73	--	--	this study
Lone Pine Creek	LPC13	120	26	--	31	--	--	this study
Kern (North Fork)	KN09	384	38	343	79	--	--	Baronas et al. (2017a)
Kern* (Lower)	KL09	596	44	430	105	--	--	Baronas et al. (2017a)
San Gabriel (North Fork)	SGN13	475	112	1063	484	--	--	Baronas et al. (2017a)
Santa Clara	SC13	5776	194	5551	3302	--	7868	this study
Hondo*	RH08	693	75	1141	606	--	411	Baronas et al. (2017a)
Los Angeles River*	LAR13	--	--	--	--	--	--	
Mackenzie	CAN10-(11+14)	309	22	994	454	184	437	Dellinger, PhD (2013)
Liard	CAN10-(46+48)	118	17.5	932	434	158	584	Dellinger, PhD (2013)
Peel	CAN10-(03+05)	183	13.8	1227	632	39	713	Dellinger, PhD (2013)
Fraser	FR15	--	--	--	--	--	--	
<u>Greenland</u>								
Watson	JO-14	51	33	--	17.2	--	--	this study
<u>Volcanic islands</u>								
Waimano	OA14-1	355	24	--	126	--	--	this study
Uhva	OA14-2	576	28	--	333	--	--	this study
Kahaua	OA14-3	420	16	--	210	--	--	this study
Molokai	ML09	--	184	377	610	--	--	Baronas et al. (2017a)
Iao Valley	MA09	247	14.6	147	130	--	--	Baronas et al. (2017a)
Ytra Ranga	YR15	--	--	--	--	--	--	
Grande Riviere de Goyave	AN-14-(42-44)	308	13.7	128	67	269	30	Gaillardet & Bouchez, unpub.
<u>Asia & Oceania</u>								
Changjiang* (Nov 2014)	CJ14	455	82	--	343	--	--	this study
Changjiang* (Jan 2015)	CJ15	678	89	818	386	--	--	this study
Mekong	ME14	404	52	910	342	--	332	this study
Nam Xong	NX14	186	12.5	1215	349	--	168	this study
Otira	OT14	56	4.8	--	13.0	--	--	this study
<u>South America</u>								
Taconazo	LS01	60	9	14	12	53	6	Baronas, West et al. (in prep.)
Kosñipata (Aug 2013)	MMD-02	127	10.2	202	131	4.0	292	Torres et al. (2016)
Kosñipata (Oct 2015)	KOS15	--	--	--	--	--	--	
Carbon	MMD-05	76	22	82	29	0.7	2.7	Torres et al. (2016)
Madre de Dios	MMD-28	92	26	344	86	5.0	54	Torres et al. (2016)
Madre de Dios	MMD-32	112	26	270	81	9.7	69	Torres et al. (2016)
Inambari	MMD-29	94	17	116	51	19.8	112	Torres et al. (2016)
Piedras	MMD-34	318	59	427	182	5.2	12.6	Torres et al. (2016)
Solimões (Jun 2005)	AM-05-(05-08)	126	23	49	212	87	29	Dellinger et al. (2015)
Solimões (Dec 2014)	AM14-36	139	27	--	58	--	--	this study
Negro	AM14-40	20.0	11.3	--	7.6	--	--	this study
Madeira	AM06-(34-43)	58	32	101	58	17	49	Bouchez, PhD (2009)
Amazon	AM06-(23-30)	103	20	47	204	83	35	Bouchez, PhD (2009)

Table B3: Sample details and dissolved composition of additional rivers.

River	Sample ID	Date	Lat., °	Long., °	Ge, pmol/L	Si, µmol/L	Ge/Si, µmol/mol	Na, µmol/L	K, µmol/L	Ca, µmol/L	Mg, µmol/L
San Jacinto, California	SJ14	2014-12-04	33.731	-116.809	18	352	0.05	626	89.6	166.7	51.8
Basse Terre, Guadeloupe	AN-14-40	2014-06-14	16.178	-61.693	70	477	0.15	352.4 ^a	18.1 ^a	139.5 ^a	89.6 ^a
<i><u>Mackenzie basin</u></i>											
Salt	CAN-09-27	2009-07-17	60.021	-112.351	46	158	0.29	35217 ^b	61.4 ^b	1646 ^b	6608 ^b
--	CAN-10-18	2010	--	--	27	51	0.53	--	--	--	--
Hay	CAN-10-59	2010	--	--	57	104	0.55	601 ^b	25.8 ^b	886 ^b	444 ^b
<i><u>Amazon basin</u></i>											
Trombetas	AM89_TR	1989-05	-1.748	-55.895	71	127	0.56	31.0 ^c	23.0 ^c	11.0 ^c	9.0 ^c
Tapajos	AM14_TA	2014-07-27	-2.373	-54.808	64	157	0.41	34.0	21.4	25.1	20.5
Obidos	AM14_00	2014-04-01	-1.943	-55.501	109	138	0.79	72.0	29.1	137.5	57.2
Obidos	AM14_01	2014-07-28	-1.943	-55.501	75	130	0.58	66.2	21.5	97.8	35.9

^a Gaillardet & Bouchez, unpublished

^b Dellinger, PhD (2013)

^c Allègre et al. (1996); Gaillardet et al. (1997); Dosseto et al. (2006); Dellinger et al.(2015)

C1 Appendix: Coupled Ge-Si isotope model: particulars

C1.1 Derivation of mixed open system equation

The system of equations describing the mass balance for the equilibrium fractionation of isotopic or elemental ratios between two phases is as follows:

$$1) R_{\text{rock}} = R_1 f_1 + R_2 f_2 \quad (\text{C1})$$

$$2) f_1 + f_2 = 1 \quad (\text{C2})$$

$$3) \alpha_1 = \frac{R_1}{R_2} \quad (\text{C3})$$

These equations can be combined:

$$R_{\text{rock}} = R_2 f_2 + \alpha_1 R_2 (1 - f_2)$$

and rearranged to solve for the ratio in one of the two phases:

$$R_2 = \frac{R_{\text{rock}}}{f_2 + \alpha_1 (1 - f_2)} \quad (\text{C4})$$

$$= \frac{R_{\text{rock}}}{\alpha_1 + f_2 (1 - \alpha_1)} \quad (\text{C5})$$

which is equivalent to Eq. 2. If phase 1 is equivalent to a precipitated solid (e.g., secondary minerals) and phase 2 remains in solution, and is then further fractionated by a second removal process (e.g., biological uptake), then an identical set of equations can be applied:

$$1) R_2 = R_{\text{diss}} f_{\text{diss}} + R_3 f_3 \quad (\text{C6})$$

$$2) f_{\text{diss}} + f_3 = f_2 \quad (\text{C7})$$

$$3) \alpha_2 = \frac{R_3}{R_{\text{diss}}} \quad (\text{C8})$$

again, yielding the composition of the final dissolved phase:

$$R_{\text{diss}} = \frac{R_2}{\alpha_2 + f_{\text{diss}} (1 - \alpha_2)} \quad (\text{C9})$$

Combining Eqs. C4 and C9 yields Eq. 4 and can alternatively be expressed as:

$$R_{\text{diss}} = \frac{R_{\text{rock}}}{\left(\alpha_1 + f_2 (1 - \alpha_1)\right) \left(\alpha_2 + \frac{f_{\text{diss}}}{f_2} (1 - \alpha_2)\right)} \quad (\text{C10})$$

Table C1: Measured Ge/Na and Si/Na ratios and calculated f_{diss} values for rivers presented in this study.

River	Sample ID	Dissolved		Sediment		$f_{\text{diss}}\text{Ge}^{\S}$	$f_{\text{diss}}\text{Si}^{\S}$
		Ge/Na	Si/Na	Ge/Na	Si/Na		
		$\mu\text{mol/mol}$	mol/mol	$\mu\text{mol/mol}$	mol/mol		
<i>Upper continental crust (UCC) (Rudnick & Gao, 2014)</i>				18.28	10.53		
<i>Average acidic rocks (Edmond et al., 1995)</i>				16.42	5.48		
Mississippi* (Aug 2011)	MI11	0.19	0.12	-	-	0.011	0.015
Mississippi* (Jul 2015)	GRO001622	0.26	0.18	-	-	0.015	0.022
Kaweah	KW13	2.36	0.72	-	-	0.136	0.090
Lone Pine Creek	LPC13	0.78	1.36	-	-	0.045	0.170
Kern (North Fork)	KN09	1.60	0.85	-	-	0.092	0.106
Kern* (Lower)	KL09	0.50	0.06	-	-	0.029	0.008
San Gabriel (North Fork)	SGN13	0.14	0.54	-	-	0.008	0.067
Santa Clara	SC13	0.03	0.07	-	-	0.002	0.009
Hondo*	RH08	0.25	0.42	-	-	0.014	0.052
Los Angeles River*	LAR13	-	-	-	-	-	-
Mackenzie	CAN10-(11+14)	0.21	0.21	-	53.6	0.012	0.026
Liard	CAN10-(46+48)	-	0.75	-	-	-	0.094
Peel	CAN10-(03+05)	0.41	0.34	-	59.2	0.024	0.042
Fraser	FR15	-	-	-	-	-	-
Watson	JO-14	1.09	0.66	9.8	7.3	0.111	0.146
Waimano	OA14-1	0.13	0.57	-	-	0.008	0.071
Uhva	OA14-2	0.16	0.85	-	-	0.009	0.107
Kahaua	OA14-3	0.47	0.95	-	-	0.027	0.119
Molokai	ML09	-	-	-	-	-	-
Iao Valley	MA09	0.49	1.43	-	-	0.028	0.179
Ytra Ranga	YR15	-	-	-	-	-	-
Grande Riviere de Goyave	AN-14-(42-44)	0.25	1.19	-	-	0.014	0.149
Changjiang* (Nov 2014)	CJ14	0.50	0.25	90.8	28.8	0.005	0.009
Changjiang* (Jan 2015)	CJ15	0.39	0.18	90.8	28.8	0.004	0.006
Mekong	ME14	0.87	0.61	110.8	38.6	0.008	0.016
Nam Xong	NX14	0.48	1.75	-	-	0.004	0.045
Otira	OT14	4.17	1.18	-	-	0.240	0.147
Taconazo	LS01	1.77	2.00	117.6	21.4	0.015	0.107
Kosñipata (Aug 2013)	MMD-02	0.71	1.86	107.4	31.6	0.007	0.052
Kosñipata (Oct 2015)	KOS15	-	-	107.4	31.6	-	-
Carbon	MMD-05	3.40	2.48	-	-	0.196	0.428
Madre de Dios	MMD-28	1.16	1.39	74.3	47.3	0.016	0.056
Madre de Dios	MMD-32	1.31	1.45	74.3	47.3	0.018	0.058
Inambari	MMD-29	2.24	1.70	-	-	0.129	0.294
Piedras	MMD-34	0.36	1.24	-	-	0.020	0.214
Solimões (Jun 2005)	AM-05-(05-08)	0.84	1.25	53.0	42.3	0.016	0.071
Solimões (Dec 2014)	AM14-36	0.96	1.11	53.0	42.3	0.018	0.063
Negro	AM14-40	3.50	4.50	-	-	0.043	0.168
Madeira	AM06-(34-43)	2.53	2.66	93.4	65.4	0.027	0.086
Amazon	AM06-(23-30)	1.15	1.40	43.3	35.1	0.027	0.097

* Affected by anthropogenic activity. The Mississippi, Hondo, and Los Angeles rivers are incorporate significant industrial and urban runoff. Changjiang chemistry is affected by extensive irrigation and farming of rice paddies in the floodplain (Ding et al., 2004). Lower Kern river was sampled downstream of a dam reservoir in which water chemistry is strongly modified by diatom growth (Baronas et al., 2017a).

[§] Calculated using Eq. 1. Where sediment data is not available, the f_{diss} range was calculated taking the intermediate X/Na value between UCC composition of Rudnick & Gao (2014) and the acidic rock (no quartz) composition of Edmond et al. (1995). The uncertainty was calculated by taking the standard error of the mean of the two values and propagating with 1σ standard deviation of dissolved Ge, Si, and Na concentration variations in rivers with multiple samples available (i.e. Mississippi, Changjiang, and Solimoes), which yielded uncertainties of 16% $f_{\text{diss}}\text{Ge}$ and 37% for $f_{\text{diss}}\text{Si}$. Where sediment data is available, the uncertainty was estimated to be 20% for $f_{\text{diss}}\text{Ge}$ and 25% for $f_{\text{diss}}\text{Si}$, propagated from sediment Ge, Si, and Na concentration variations with depth in Madeira river (see Table B1) and from the same 1σ uncertainties of dissolved concentrations. It was assumed that the higher uncertainty (20% for $f_{\text{diss}}\text{Ge}$ and 37% for $f_{\text{diss}}\text{Si}$) applies to all catchments.

which is the 2-stage fractionation equation used by Hofmann (1988) to model crust-mantle differentiation. It could be expressed in our case, e.g., for Si isotope fractionation in the critical zone as:

$$R_{\text{diss}}^{30/28} = \frac{R_{\text{rock}}^{30/28}}{\left(\alpha_{\text{sec}}^{30/28} + (1 - f_{\text{sec}}^{\text{Si}})(1 - \alpha_{\text{sec}}^{30/28})\right) \left(\alpha_{\text{bio}}^{30/28} + \frac{f_{\text{diss}}^{\text{Si}}}{1 - f_{\text{sec}}^{\text{Si}}} (1 - \alpha_{\text{bio}}^{30/28})\right)} \quad (\text{C11})$$

C1.2 Monte Carlo routine

To assess the uncertainty of the calculated parameters, a Monte Carlo approach is used, where the input parameters are selected randomly from within a defined probability distribution and the calculation routine described in the main text (Section 3.4.1 is repeated many times, to obtain a robust uncertainty range of the calculated parameters. The data used to calculate $f_{\text{diss}}^{\text{X}}$ values and their uncertainties are given in Table C1. The ranges and probability distributions of the other input parameters are given in Table C2. Within individual Monte Carlo runs, certain parameter combinations can yield physically impossible values (e.g., $f_i^{\text{Si}} < 0$ or > 1). These runs are therefore discarded.

For some of the samples, the $\alpha_{\text{sec}}^{\text{Ge/Si}}$ range of 1.2-3 based on the studies of Murnane & Stallard (1990) and Froelich et al. (1992) did not yield any feasible f_{sec} and f_{bio} values, suggesting that the parameter space is insufficient to explain the Ge/Si fractionation during weathering in these watersheds. In these cases, the range of allowed $\alpha_{\text{sec}}^{\text{Ge/Si}}$ was extended up to 30. This range is justified given previous observations of very Ge-rich and Si-poor secondary phases with Ge/Si ratios reaching above 10 $\mu\text{mol/mol}$ in allophane and upwards of 100 $\mu\text{mol/mol}$ in Fe/Al-(oxy)hydroxides (Kurtz et al., 2002; Scribner et al., 2006).

Table C2: The ranges of input values used in the model. Δ fractionation factors refer to both Δ_{sec} and Δ_{bio} .

River	Sample ID	Ge/Si _{rock} , $\mu\text{mol/mol}$	$\delta^{30}\text{Si}_{\text{rock}}$, ‰	$\delta^{74}\text{Ge}_{\text{rock}}$, ‰	$\Delta^{30}\text{Si}$, ‰ ^f	$\Delta^{74}\text{Ge}$, ‰ ^g	$\alpha^{\text{Ge/Si}}_{\text{bio}}$ ^h	$\alpha^{\text{Ge/Si}}_{\text{sec}}$ ⁱ
	<i>prob. distrib.</i>	<i>normal</i>	<i>normal</i>	<i>normal</i>	<i>uniform</i>	<i>uniform</i>	<i>uniform</i>	<i>uniform</i>
Mississippi* (Jul 2015)	GRO001622	2.2 ± 0.5 ^a	-0.25 ± 0.08 ^d	0.58 ± 0.10 ^e	-3 to 0	-6 to 6	0.005 - 0.56	1.2 - 3
Kern* (Lower)	KL09	2.2 ± 0.5 ^a	-0.25 ± 0.08 ^d	0.58 ± 0.10 ^e	-6 to 0 / -3 to 0 ^j	-6 to 6	0.005 - 0.56	1.2 - 3
San Gabriel (North Fork)	SGN13	2.2 ± 0.5 ^a	-0.25 ± 0.08 ^d	0.58 ± 0.10 ^e	-3 to 0	-6 to 6	0.005 - 0.56	1.2 - 30
Mackenzie	CAN10-(11+14)	2.2 ± 0.5 ^a	-0.25 ± 0.08 ^d	0.58 ± 0.10 ^e	-3 to 0	-6 to 6	0.005 - 0.56	1.2 - 3
Liard	CAN10-(46+48)	2.2 ± 0.5 ^a	-0.25 ± 0.08 ^d	0.58 ± 0.10 ^e	-3 to 0	-6 to 6	0.005 - 0.56	1.2 - 3
Peel	CAN10-(03+05)	2.2 ± 0.5 ^a	-0.25 ± 0.08 ^d	0.58 ± 0.10 ^e	-3 to 0	-6 to 6	0.005 - 0.56	1.2 - 3
Watson	JO-14	2.2 ± 0.5 ^a	-0.25 ± 0.08 ^d	0.58 ± 0.10 ^e	-3 to 0	-6 to 6	0.005 - 0.56	1.2 - 3
Uhva	OA14-2	2.2 ± 0.5 ^a	-0.25 ± 0.08 ^d	0.58 ± 0.10 ^e	-3 to 0	-6 to 6	0.005 - 0.56	1.2 - 30
Grande Riviere de Goyave	AN-14-(42-44)	2.2 ± 0.5 ^a	-0.25 ± 0.08 ^d	0.58 ± 0.10 ^e	-3 to 0	-6 to 6	0.005 - 0.56	1.2 - 30
Taconazo	LS01	6.3 ± 1.0 ^b	-2.07 ± 0.25 ^b	-0.12 ± 0.12 ^b	-3 to 0	-6 to 6	0.005 - 0.56	1.2 - 30
Kosñipata (Aug 2013)	MMD-02	3.0 ± 1.0 ^c	-0.40 ± 0.20 ^c	0.58 ± 0.10 ^e	-3 to 0	-6 to 6	0.005 - 0.56	1.2 - 3
Madre de Dios	MMD-28	3.0 ± 1.0 ^c	-0.40 ± 0.20 ^c	0.58 ± 0.10 ^e	-3 to 0	-6 to 6	0.005 - 0.56	1.2 - 3
Madre de Dios	MMD-32	3.0 ± 1.0 ^c	-0.40 ± 0.20 ^c	0.58 ± 0.10 ^e	-3 to 0	-6 to 6	0.005 - 0.56	1.2 - 3
Inambari	MMD-29	3.0 ± 1.0 ^c	-0.40 ± 0.20 ^c	0.58 ± 0.10 ^e	-3 to 0	-6 to 6	0.005 - 0.56	1.2 - 3
Piedras	MMD-34	3.0 ± 1.0 ^c	-0.40 ± 0.20 ^c	0.58 ± 0.10 ^e	-3 to 0	-6 to 6	0.005 - 0.56	1.2 - 30
Solimões (Dec 2014)	AM14-36	3.0 ± 1.0 ^c	-0.40 ± 0.20 ^c	0.58 ± 0.10 ^e	-3 to 0	-6 to 6	0.005 - 0.56	1.2 - 3
Negro	AM14-40	3.0 ± 1.0 ^c	-0.40 ± 0.20 ^c	0.58 ± 0.10 ^e	-3 to 0	-6 to 6	0.005 - 0.56	1.2 - 3
Amazon	AM06-(23-30)	3.0 ± 1.0 ^c	-0.40 ± 0.20 ^c	0.58 ± 0.10 ^e	-3 to 0	-6 to 6	0.005 - 0.56	1.2 - 3

^a Average of Rudnick & Gao (2014) and Edmond et al. (1995)

^b Baronas et al. (in prep.)

^c Average of suspended river sediment in the Amazon system (Peruvian rivers and Madeira).

^d UCC composition from Savage et al. (2013)

^e UCC composition from Rouxel & Luais (2017)

^f Conservative range encompassing the compilation by Frings et al. (2016)

^g Extremely conservative range due to lack of experimental data, encompassing values determined by Li & Liu (2010) and Pokrovsky et al. (2016)

^h Encompassing the range reported by Derry et al. (2006), Blecker et al. (2007), Meek et al. (2016).

ⁱ Encompassing the range reported by Murnane & Stallard (1990) and Froelich et al. (1992). Additional justification for values up to 30 given in the text.

^j The ranges used in Rayleigh / Mixed Open System models, respectively (see text for detailed discussion of sample KL09).

C1.3 Model results

The above-described Monte Carlo routine was repeated 10^6 times for each sample where all required data was available. After selecting only those runs which reproduced the measured $\delta^{30}\text{Si}_{\text{diss}}$ and $\delta^{74}\text{Ge}_{\text{diss}}$ values within analytical uncertainty, anywhere between 400-6000 runs were retained, depending on the river (Table C3). The reproducibility of the results was checked by doing repeat runs with a smaller range of allowed $\Delta^{74}\text{Ge}$ values, which resulted in about twice the number of retained values. There was no difference in the median and standard deviation values of the calculated parameters for which $\Delta^{74}\text{Ge}$ had no influence (e.g., f_{sec} , f_{bio} , $\Delta^{30}\text{Si}$, etc.). An example of the distribution of input parameters (Fig. C1) and the calculated values (Figs C2 and C3) is given for the Mackenzie river (CAN10-(11+14)). The modeling results of all samples are summarized in Table C3 and Figs C4 and C5.

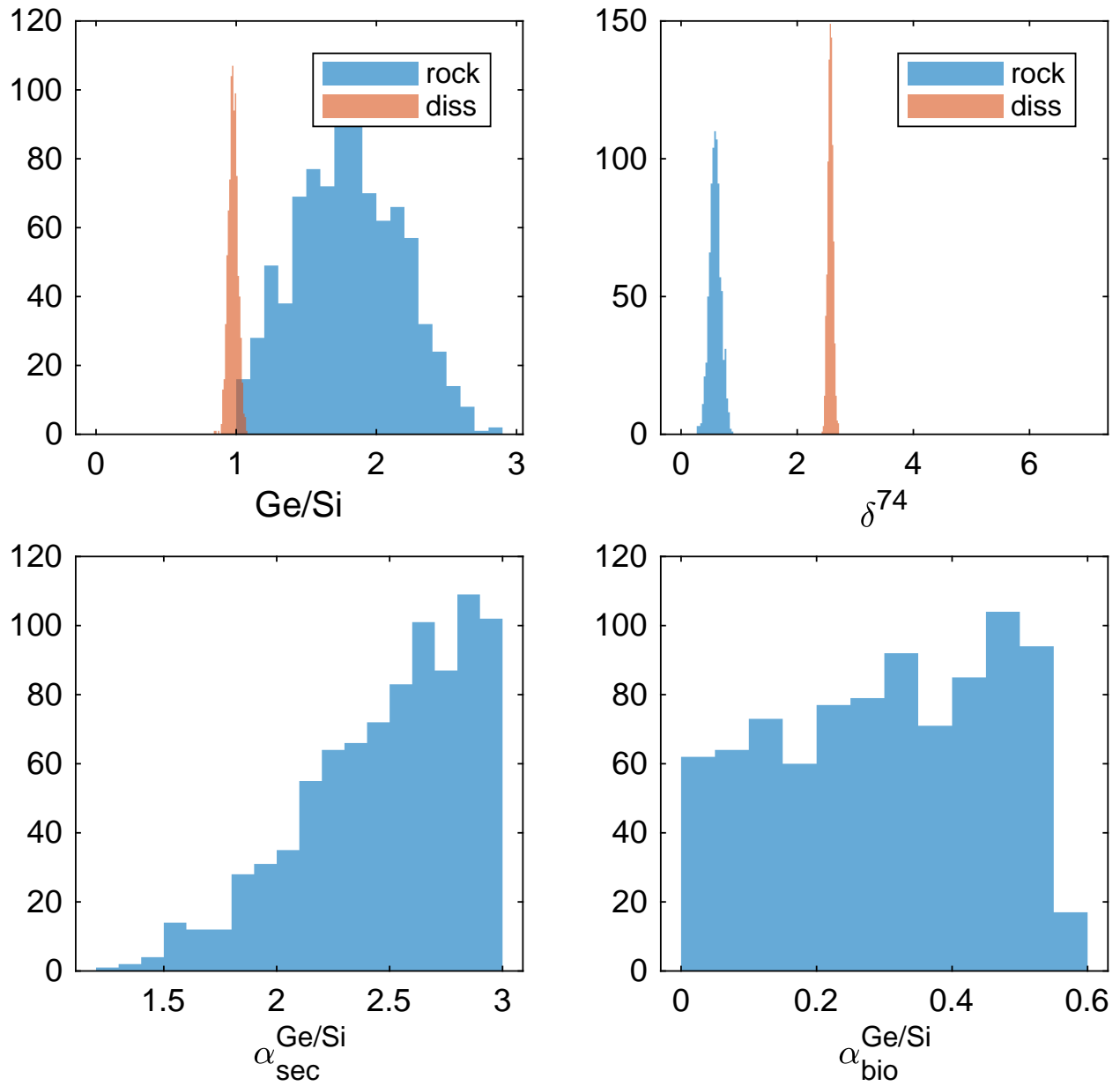


Figure C1: Distributions of input parameters used in modeling the Mackenzie River (CAN10-(11+14)) retained after the Monte Carlo routine.

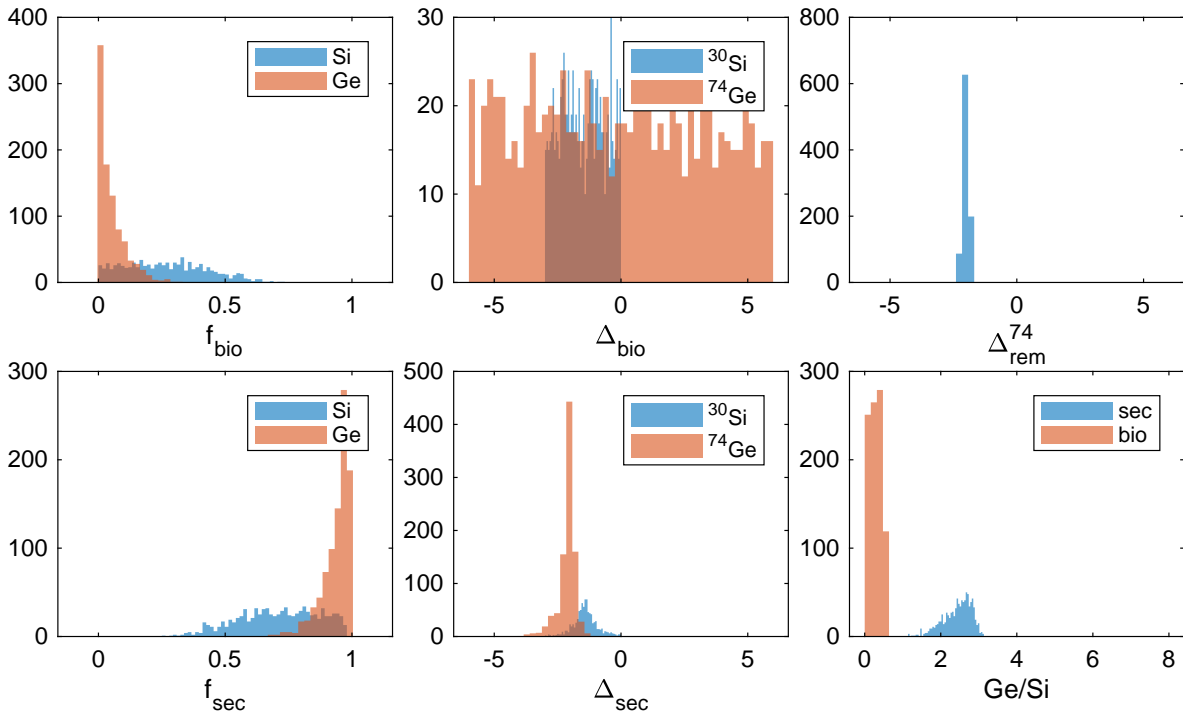


Figure C2: Distributions of model results for the Mackenzie River (CAN10-(11+14)) retained after the Monte Carlo routine. Δ_{rem}^{74} refers to the Ge isotope fractionation factor, without distinguishing between secondary (sec) or biological (bio) fractionation.

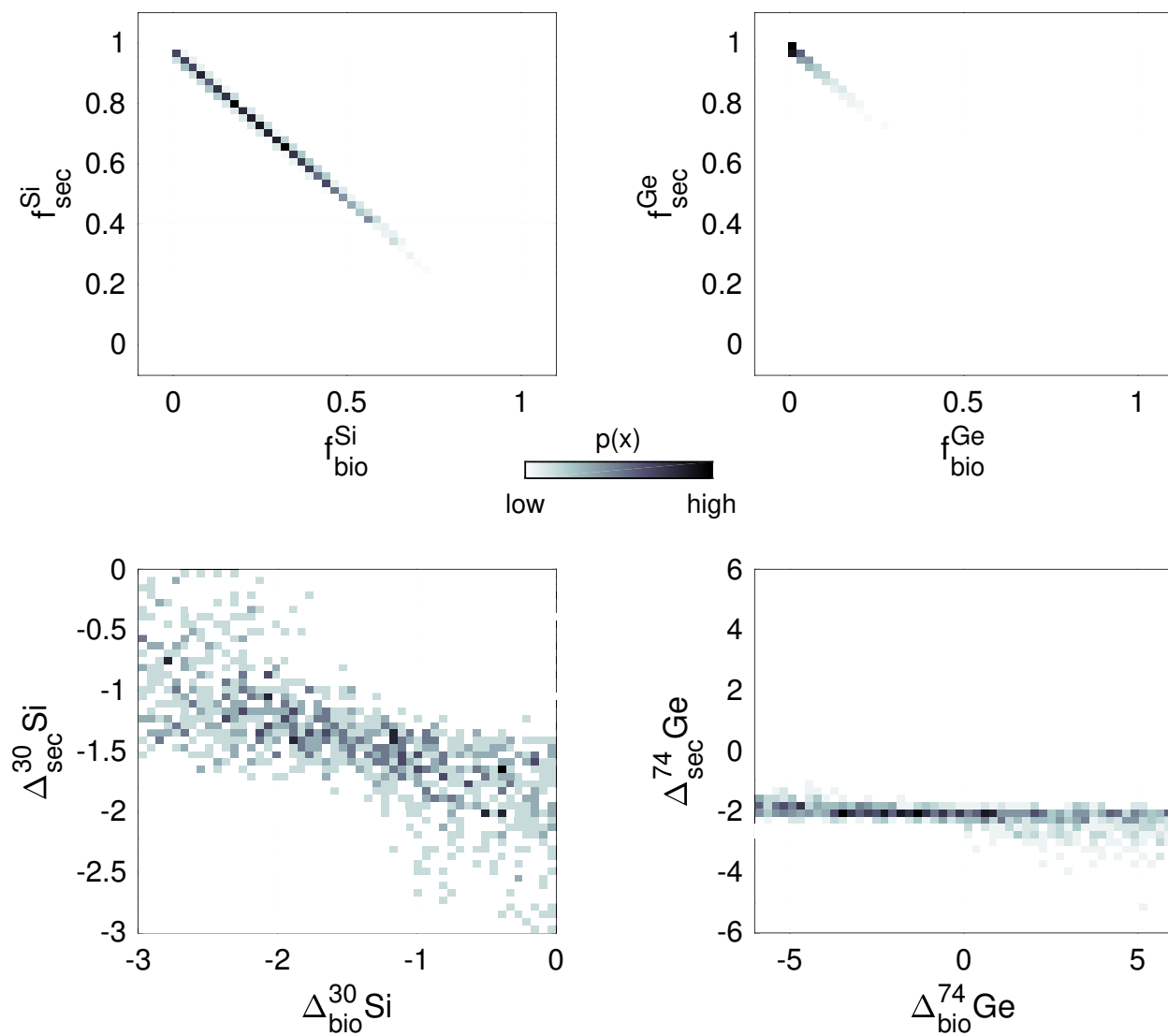


Figure C3: Probability distribution heatmaps (2D histograms) of model results for the Mackenzie River (CAN10-(11+14)) retained after the Monte Carlo routine. Darker color indicates higher probability density $p(x)$.

Table C3: Model results. The uncertainty is reported as $\pm 1\sigma$ (25-75th percentile). Note that in some cases the calculated (*a posteriori*) parameters span the whole pre-assigned (*a priori*) range as given in Table C2 (e.g., $\Delta^{30}\text{Si}_{\text{sec}}$ for KL09 or $\Delta^{74}\text{Ge}_{\text{bio}}$ for all samples, with the exception of KL09 "dam only" run), meaning that the model is unable to narrow down the range of possible values for those parameters.

River	Sample ID	model	n	f_{bioSi}	f_{secSi}	f_{bioGe}	f_{secGe}	$\Delta^{30}\text{Si}_{\text{bio}}$	$\Delta^{30}\text{Si}_{\text{sec}}$	$\Delta^{74}\text{Ge}_{\text{bio}}$	$\Delta^{74}\text{Ge}_{\text{sec}}$	$\text{Ge/Si}_{\text{bio}}$	$\text{Ge/Si}_{\text{sec}}$
Mississippi* (Jul 2015)	GRO001622	mixed open system	6243	0.4 ± 0.19 (0.27-0.54)	0.58 ± 0.19 (0.44-0.71)	0.07 ± 0.1 (0.03-0.14)	0.91 ± 0.1 (0.84-0.96)	-1.88 ± 0.76 (-2.40 - -1.28)	-2.04 ± 0.60 (-2.40 - -1.67)	0.12 ± 3.44 (-2.88-3.08)	-2.17 ± 0.73 (-2.49 - -1.91)	0.43 ± 0.23 (0.22-0.63)	3.36 ± 0.69 (2.79-3.88)
Kern* (Lower)	KL09	mixed open system	4827	0.93 ± 0.05 (0.89-0.96)	0.07 ± 0.05 (0.04-0.1)	0.44 ± 0.27 (0.23-0.68)	0.53 ± 0.27 (0.29-0.74)	-4.60 ± 0.25 (-4.75 - -4.45)	-3.00 ± 1.75 (-4.51 - -1.49)	-2.13 ± 2.86 (-3.53-0.10)	-2.35 ± 2.71 (-3.64 - -0.67)	1.06 ± 0.67 (0.58-1.60)	17.04 ± 4.35 (13.48-20.96)
Kern* (Lower)	KL09	m.o.s. + rayleigh	1521	0.86 ± 0.05 (0.82-0.9)	0.14 ± 0.05 (0.1-0.17)	0.38 ± 0.2 (0.24-0.55)	0.59 ± 0.2 (0.42-0.74)	-2.18 ± 0.38 (-2.46 - -1.89)	-1.57 ± 0.87 (-2.32 - -0.79)	-1.87 ± 1.52 (-3.21 - -0.99)	-2.14 ± 1.34 (-2.99 - -1.29)	0.47 ± 0.30 (0.29-0.69)	9.42 ± 2.88 (7.89-11.18)
Kern* (Lower)	KL09	rayleigh (dam only)	11783	0.85 ± 0.08 (0.79-0.9)	-	0.4 ± 0.1 (0.34-0.47)	-	-	-	-0.70 ± 0.72 (-1.19 - -0.33)	-	0.82 ± 0.34 (0.53-1.07)	-
San Gabriel (North Fork)	SGN13	mixed open system	5578	0.52 ± 0.21 (0.31-0.64)	0.41 ± 0.21 (0.3-0.62)	0.01 ± 0.02 (0.01-0.03)	0.98 ± 0.02 (0.96-0.99)	-2.53 ± 0.59 (-2.77 - -2.20)	-2.52 ± 0.52 (-2.76 - -2.15)	-0.11 ± 3.49 (-3.09-3.03)	-4.94 ± 0.38 (-5.23 - -4.62)	0.08 ± 0.04 (0.04-0.11)	4.99 ± 1.77 (3.46-6.56)
Mackenzie	CAN10-(11+14)	mixed open system	914	0.26 ± 0.16 (0.13-0.39)	0.72 ± 0.16 (0.59-0.84)	0.03 ± 0.05 (0.01-0.07)	0.96 ± 0.05 (0.92-0.98)	-1.50 ± 0.85 (-2.24 - -0.79)	-1.42 ± 0.48 (-1.67 - -1.17)	-0.10 ± 3.43 (-3.10-2.80)	-2.06 ± 0.36 (-2.20 - -1.94)	0.29 ± 0.16 (0.14-0.41)	2.50 ± 0.37 (2.19-2.72)
Liard	CAN10-(46+48)	mixed open system	399	0.16 ± 0.12 (0.08-0.26)	0.78 ± 0.11 (0.69-0.86)	0.02 ± 0.03 (0.01-0.04)	0.95 ± 0.03 (0.93-0.97)	-1.61 ± 0.87 (-2.23 - -0.76)	-1.23 ± 0.33 (-1.41 - -1.03)	0.26 ± 3.50 (-2.59-3.41)	-2.30 ± 0.25 (-2.44 - -2.12)	0.19 ± 0.10 (0.10-0.27)	1.74 ± 0.18 (1.60-1.84)
Peel	CAN10-(03+05)	mixed open system	1629	0.32 ± 0.17 (0.19-0.45)	0.64 ± 0.17 (0.51-0.77)	0.05 ± 0.07 (0.02-0.11)	0.93 ± 0.07 (0.87-0.96)	-1.42 ± 0.82 (-2.11 - -0.74)	-1.21 ± 0.55 (-1.50 - -0.89)	-0.10 ± 3.45 (-3.08-2.79)	-2.88 ± 0.51 (-3.12 - -2.74)	0.37 ± 0.19 (0.20-0.52)	2.95 ± 0.52 (2.52-3.32)
Watson	JO-14	mixed open system	1555	0.35 ± 0.22 (0.16-0.53)	0.5 ± 0.2 (0.34-0.66)	0.06 ± 0.13 (0.02-0.16)	0.82 ± 0.13 (0.73-0.86)	-0.28 ± 0.60 (-0.61 - -0.12)	-0.21 ± 0.30 (-0.38 - -0.10)	0.05 ± 3.46 (-2.98-3.05)	-0.33 ± 1.09 (-0.60 - -0.06)	0.50 ± 0.27 (0.26-0.72)	3.61 ± 0.83 (2.91-4.26)
Uhva	OA14-2	mixed open system	4495	0.37 ± 0.16 (0.25-0.48)	0.52 ± 0.15 (0.42-0.64)	0.01 ± 0.01 (0-0.01)	0.98 ± 0.01 (0.98-0.99)	-1.32 ± 0.80 (-1.97 - -0.66)	-1.23 ± 0.63 (-1.65 - -0.80)	0.03 ± 3.44 (-2.95-2.96)	-3.00 ± 0.20 (-3.15 - -2.85)	0.05 ± 0.03 (0.03-0.08)	4.10 ± 0.98 (3.27-4.82)
Grande Riviere de Goyave	AN-14-(42-44)	mixed open system	4547	0.38 ± 0.16 (0.25-0.49)	0.47 ± 0.15 (0.38-0.59)	0.01 ± 0.01 (0-0.02)	0.98 ± 0.01 (0.97-0.98)	-1.64 ± 0.78 (-2.24 - -1.04)	-1.76 ± 0.68 (-2.20 - -1.32)	0.00 ± 3.43 (-2.90-3.00)	-3.08 ± 0.19 (-3.21 - -2.94)	0.06 ± 0.03 (0.03-0.09)	4.50 ± 1.13 (3.56-5.35)
Taconazo	LS01	mixed open system	894	0.55 ± 0.2 (0.36-0.64)	0.34 ± 0.19 (0.26-0.53)	0.02 ± 0.02 (0.01-0.03)	0.97 ± 0.02 (0.95-0.98)	-2.54 ± 0.57 (-2.81 - -2.17)	-2.40 ± 0.62 (-2.73 - -1.93)	0.01 ± 3.50 (-3.15-2.91)	-2.79 ± 0.18 (-2.91 - -2.67)	0.26 ± 0.14 (0.13-0.38)	17.21 ± 5.98 (11.72-22.06)
Koshipata (Aug 2013)	MMD-02	mixed open system	4475	0.53 ± 0.19 (0.39-0.65)	0.41 ± 0.18 (0.31-0.55)	0.02 ± 0.02 (0.01-0.03)	0.98 ± 0.02 (0.96-0.99)	-1.38 ± 0.70 (-1.89 - -0.91)	-1.42 ± 0.76 (-2.00 - -0.89)	-0.11 ± 3.46 (-3.04-2.97)	-4.47 ± 0.22 (-4.61 - -4.33)	0.11 ± 0.06 (0.05-0.16)	7.31 ± 2.41 (5.41-9.26)
Madre de Dios	MMD-28	mixed open system	496	0.2 ± 0.16 (0.09-0.35)	0.77 ± 0.15 (0.62-0.87)	0.02 ± 0.05 (0.01-0.05)	0.96 ± 0.05 (0.93-0.98)	-1.40 ± 0.83 (-2.21 - -0.79)	-1.24 ± 0.45 (-1.48 - -0.97)	0.30 ± 3.50 (-2.53-3.36)	-2.78 ± 0.34 (-2.96 - -2.65)	0.24 ± 0.14 (0.11-0.35)	2.17 ± 0.32 (1.90-2.36)
Madre de Dios	MMD-32	mixed open system	705	0.24 ± 0.17 (0.11-0.39)	0.72 ± 0.17 (0.58-0.85)	0.03 ± 0.06 (0.01-0.07)	0.95 ± 0.06 (0.91-0.97)	-1.55 ± 0.86 (-2.22 - -0.79)	-1.51 ± 0.55 (-1.81 - -1.20)	0.19 ± 3.47 (-2.96-3.03)	-3.28 ± 0.41 (-3.47 - -3.13)	0.27 ± 0.14 (0.14-0.38)	2.36 ± 0.36 (2.05-2.57)
Inambari	MMD-29	mixed open system	2076	0.26 ± 0.18 (0.13-0.4)	0.54 ± 0.14 (0.43-0.64)	0.04 ± 0.08 (0.01-0.09)	0.83 ± 0.08 (0.78-0.85)	-1.41 ± 0.80 (-2.05 - -0.77)	-1.45 ± 0.62 (-1.84 - -1.06)	0.00 ± 3.44 (-3.02-3.00)	-3.11 ± 0.59 (-3.39 - -2.90)	0.39 ± 0.21 (0.20-0.56)	3.26 ± 0.6 (2.75-3.64)
Piedras	MMD-34	mixed open system	2421	0.35 ± 0.2 (0.18-0.51)	0.45 ± 0.16 (0.33-0.59)	0.01 ± 0.02 (0-0.02)	0.97 ± 0.02 (0.96-0.98)	-2.19 ± 0.71 (-2.60 - -1.64)	-2.40 ± 0.64 (-2.71 - -1.96)	-0.01 ± 3.48 (-2.99-3.06)	-4.25 ± 0.20 (-4.38 - -4.13)	0.08 ± 0.05 (0.04-0.12)	5.99 ± 1.69 (4.65-7.28)
Solimões (Dec 2014)	AM14-36	mixed open system	639	0.23 ± 0.16 (0.11-0.36)	0.74 ± 0.16 (0.61-0.85)	0.03 ± 0.05 (0.01-0.06)	0.95 ± 0.05 (0.92-0.97)	-1.46 ± 0.85 (-2.22 - -0.73)	-1.48 ± 0.52 (-1.75 - -1.18)	-0.17 ± 3.42 (-3.16-2.78)	-1.49 ± 0.39 (-1.69 - -1.31)	0.26 ± 0.14 (0.14-0.38)	2.26 ± 0.34 (1.98-2.45)
Negro	AM14-40	mixed open system	441	0.19 ± 0.14 (0.09-0.31)	0.72 ± 0.13 (0.61-0.82)	0.02 ± 0.04 (0.01-0.05)	0.93 ± 0.04 (0.9-0.95)	-1.52 ± 0.86 (-2.20 - -0.71)	-0.96 ± 0.45 (-1.23 - -0.65)	0.04 ± 3.49 (-3.06-3.09)	-1.53 ± 0.31 (-1.72 - -1.36)	0.22 ± 0.12 (0.12-0.32)	2.02 ± 0.30 (1.75-2.21)
Amazon	AM06-(23-30)	mixed open system	2338	0.67 ± 0.18 (0.53-0.76)	0.22 ± 0.17 (0.15-0.35)	0.04 ± 0.05 (0.02-0.08)	0.93 ± 0.05 (0.9-0.95)	-1.42 ± 0.54 (-1.75 - -1.08)	-1.49 ± 0.82 (-2.17 - -0.80)	0.02 ± 3.40 (-2.90-3.06)	-2.09 ± 0.39 (-2.25 - -1.95)	0.23 ± 0.13 (0.12-0.33)	12.82 ± 5.97 (8.06-18.00)

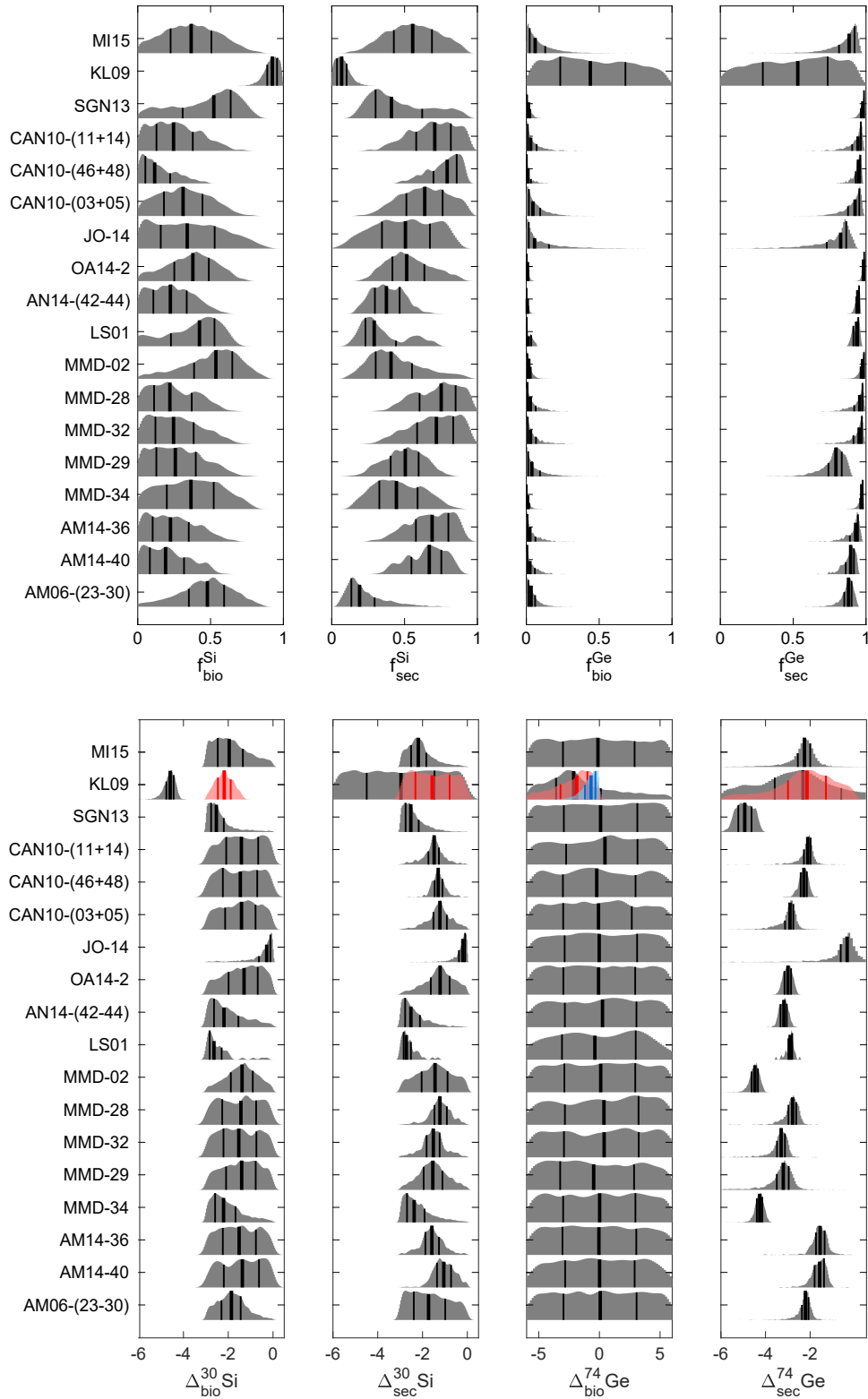


Figure C4: Probability distributions of calculated parameters for all modeled rivers. For Lower Kern (KL09), the red distributions are calculated using Rayleigh equations for the biological uptake step and the blue distributions are calculated using Rayleigh equations to calculate only biological uptake in the dam reservoir (Table C3), using measured $\delta^{74}\text{Ge}_{\text{diss}}$ of incoming rivers (North and South Fork Kern, Baronas et al. (2017a)) as an additional constraint, yielding a much more precise calculation of $\Delta^{74}\text{Ge}_{\text{bio}}$.

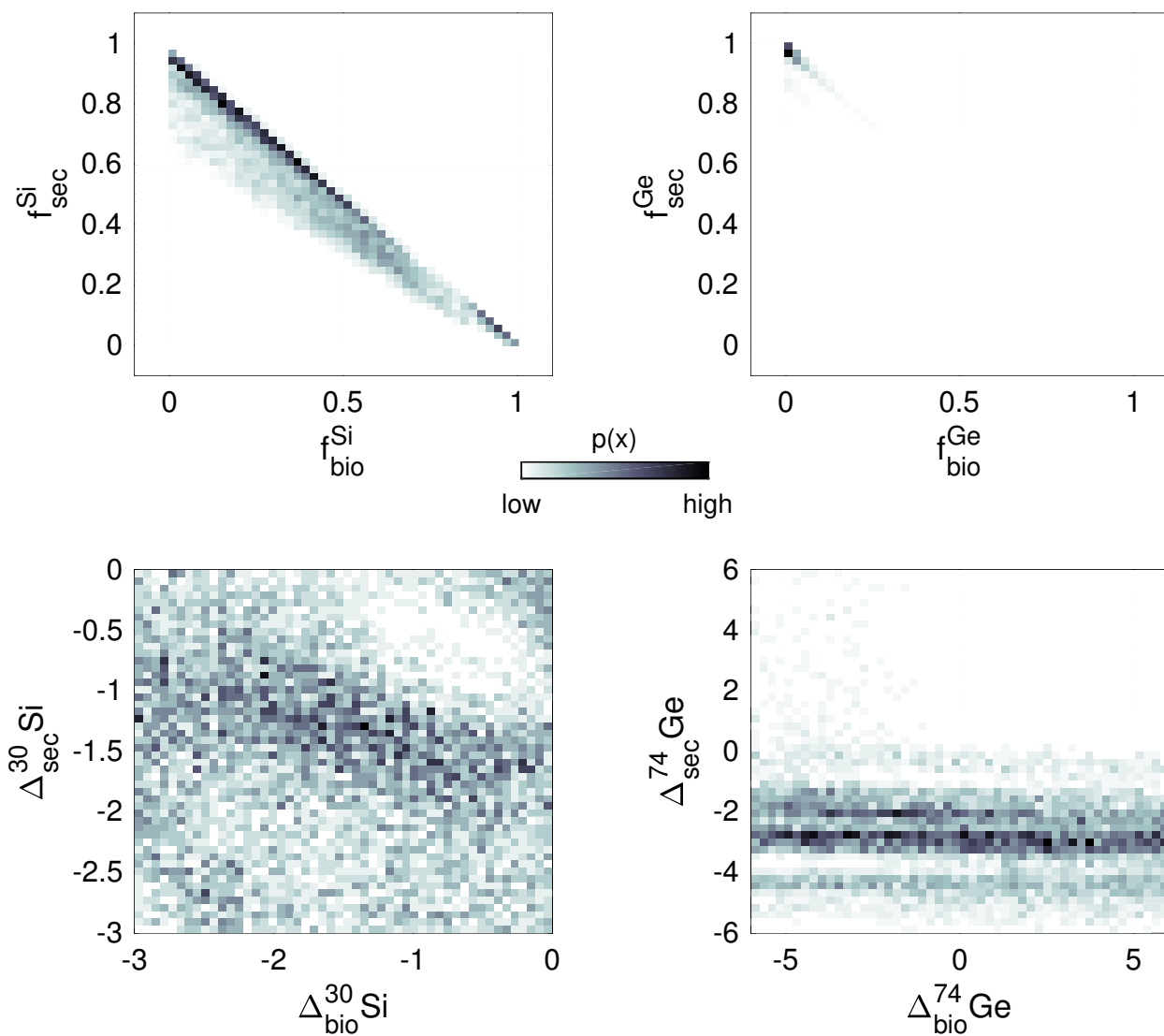


Figure C5: Probability distribution heatmaps (2D histograms) of calculated parameters for all modeled rivers (normalized to equal density).

Appendix references

- Allègre CJ, Dupré B, Négrel P, Gaillardet J, All CJ, Dupr B, Philippe N, Gaillardet J (1996) Sr-Nd-Pb isotope systematics in Amazon and Congo River systems : Constraints about erosion processes. *Chemical Geology* 131:93 – 112.
- Baronas JJ, Hammond DE, Berelson WM, McManus J, Severmann S (2016) Germanium-silicon fractionation in a river-influenced continental margin: The Northern Gulf of Mexico. *Geochimica et Cosmochimica Acta* 178:124–142.
- Baronas JJ, Hammond DE, McManus J, Wheat CG, Siebert C (2017) A global Ge isotope budget. *Geochimica et Cosmochimica Acta* 203:265–283.
- Dellinger M, Gaillardet J, Bouchez J, Calmels D, Louvat P, Dosseto A, Gorge C, Alanoca L, Maurice L (2015) Riverine Li isotope fractionation in the Amazon River basin controlled by the weathering regimes. *Geochimica et Cosmochimica Acta* 164:71–93.
- Dosseto A, Bourdon B, Gaillardet J, Allègre C, Filizola N (2006) Time scale and conditions of weathering under tropical climate: Study of the Amazon basin with U-series. *Geochimica et Cosmochimica Acta* 70:71–89.
- Escoube R, Rouxel OJ, Edwards K, Glazer B, Donard OFX (2015) Coupled Ge/Si and Ge isotope ratios as geochemical tracers of seafloor hydrothermal systems: Case studies at Loihi Seamount and East Pacific Rise 9°50'N. *Geochimica et Cosmochimica Acta* 167:93–112.
- Escoube R, Rouxel OJ, Luais B, Ponzevera E, Donard OF (2012) An Intercomparison Study of the Germanium Isotope Composition of Geological Reference Materials. *Geostandards and Geoanalytical Research* 36:149–159.
- Gaillardet J, Dupre B, Allegre C, Négrel P (1997) Chemical and physical denudation in the Amazon River Basin. *Chemical Geology* 142:141–173.
- Georg R, Reynolds B, Frank M, Halliday A (2006) New sample preparation techniques for the determination of Si isotopic compositions using MC-ICPMS. *Chemical Geology* 235:95–104.
- Georg R, Zhu C, Reynolds B, Halliday A (2009) Stable silicon isotopes of groundwater, feldspars, and clay coatings in the Navajo Sandstone aquifer, Black Mesa, Arizona, USA. *Geochimica et Cosmochimica Acta* 73:2229–2241.
- Hammond DE, McManus J, Berelson WM, Meredith C, Klinkhammer P, Coale K (2000) Diagenetic fractionation of Ge and Si in reducing sediments: the missing Ge sink and a possible mechanism to cause glacial/interglacial variations in oceanic Ge/Si. *Geochimica et Cosmochimica Acta* 64:2453–2465.
- Mortlock R, Froelich P (1996) Determination of germanium by isotope dilution-hydride generation inductively coupled plasma mass spectrometry. *Analytica Chimica Acta* 332:277–284.
- Mullin J, Riley J (1955) The colorimetric determination of silicate with special reference to sea and natural waters. *Analytica Chimica Acta* 12:162–175.

- Rouxel O, Galy A, Elderfield H (2006) Germanium isotopic variations in igneous rocks and marine sediments. *Geochimica et Cosmochimica Acta* 70:3387–3400.
- Siebert C, Nägler T, Kramers J (2001) Determination of molybdenum isotope fractionation by double-spike multicollector inductively coupled plasma mass spectrometry. *Geochemistry Geophysics Geosystems* 2.
- Torres MA, West AJ, Clark KE, Paris G, Bouchez J, Ponton C, Feakins SJ, Galy V, Adkins JF (2016) The acid and alkalinity budgets of weathering in the Andes–Amazon system: Insights into the erosional control of global biogeochemical cycles. *Earth and Planetary Science Letters* 450:381–391.